MACROMOLECULAR MIGRATION IN MICROFLUIDICS

By

Steacy J. Coombs

A thesis submitted to the Graduate Program in Chemical Engineering

in conformity with the requirements for the

Degree of Doctor of Philosophy

Queen's University

Kingston, Ontario, Canada

April 2024

Abstract

One of the great fascinations chemical engineers have with polymeric liquids is their curious behaviour when confined. In this thesis, we use macromolecular theory that relies entirely on flow orientation to explain the rheology of polymeric liquids in confinement. Specifically, we use rigid dumbbell theory to explain the curious effects of polymer confinement: (a) diminishing complex viscosity, and (b) emigration from high-shear.

Whereas much is known about the complex viscosity of polymeric liquids, far less is understood about the behaviour of this material function when macromolecules are confined. By *confined*, we mean that the gap along the velocity gradient is small enough to reorient the polymers. In the first part of this thesis, we examine classical analytical solutions for a confined rigid dumbbell suspension in small-amplitude oscillatory shear flow. We test these analytical solutions against the measured effects of confinement on both parts of the complex viscosity of a Carbopol suspension and three polystyrene solutions.

Microfluidic design, fabrication and experiments have developed rapidly, leading to lab-on-chip separation or fractionation. In the second part of this thesis, we design a continuous concentrator for macromolecular solutions. Our design relies on the analytical solutions for orientational diffusion under laminar pressure-driven slot flow through a microchannel. Using rigid dumbbell theory, we provide analytical solutions for the design of our microfluidic macromolecular hydrodynamic chromatography. We arrive at our design through the use of well-known confinement-driven composition profiles. Using a pair of razor-sharp blades, our design separates the slot flow into a symmetric core inner slot (concentrated) between two outer slots (diluted). We discover a minimum dimensionless blade leading edge separation for complete fractionation,

and that this decreases with confinement, and also decreases with dimensionless shear rate.

In the last part of this thesis, using our earlier analytical rigid dumbbell theory for orientational diffusion under laminar pressure-driven slot flow through a microchannel, we design and fabricate a passive, continuous microfluidic separator. By *passive*, we mean channel geometry or particle inertia control the migration inside the microchannels. We designed and fabricated (soft lithography) slot-flow and square duct straight microfluidic channels with one inlet and three outlets.

Co-Authorship

Chapter 2 and Chapter 3 has been published in a peer-reviewed journal and was supervised by Professor A. Jeffrey Giacomin. The experimental measurements presented in Chapter 2 were conducted by Dr. Rossana Pasquino from the Department of Chemical, Materials and Industrial Production Engineering (DICMaPI), University of Naples Federico II, Italy. In Chapter 3, Dr. K Tontiwattanakul, from the Department of Mechanical and Aerospace Engineering, King Mongkut's University of Technology of Thailand, contributed Figure 13. The work within Chapter 4 was conducted under the supervision of Professor Carlos Escobedo.

Acknowledgement

This research was undertaken, in part, thanks to funding from the Canada Research Chairs program of the Government of Canada of the Tier 1 Canada Research Chair in Rheology. A.J. Giacomin is indebted to the Faculty of Applied Science and Engineering of Queen's University at Kingston, for their support through a Research Initiation Grant (RIG). This research was also undertaken, in part, thanks to support from the Society of Plastics Engineers in the form of the Lew Erwin Extrusion Division Scholarship.

To my supervisor, Dr. A. Jeffrey Giacomin, thank you for sharing your endless passion for research and for your support during my doctoral studies. As an advisor and mentor, you can cut the mustard. You have become my friend, my family, and one of my favourite people over these years. I will miss being your student. Also, to my colleague in the Polymers Research Group, Dr. Mona Kanso for her patience and guidance.

To my interim supervisor, Dr. Carlos Escobedo, thank you for helping me through a difficult transition during my graduate studies. Your support and guidance in my experimental work has been invaluable.

To my parents, thank you for supporting me and asking questions, even when you have no idea what I'm talking about. You ingrained the importance of academics into me, and I would not be here without you.

And finally, to my Patrick, I dedicate this thesis to you. I love you.

CONTENTS

FIGURES

TABLES

Table 1: Dimensional Variables.

Name	Symbol	Dimension
Angular Frequency	ω	t^{-1}
Area	A	L^2
Bead Diameter	d	M
Bead Fraction Coefficient	ξ	M/t
Boltzmann's Constant	k	$\frac{M}{L^2 t^2 T}$/dumbbell
Blade Position	y_i	L
Center Position of Rigid Dumbbell	z	L
Complex Viscosity	η^*	M/Lt
Concentration, Cornet Critical	c^*	M/L^3
Concentration, Mass	c	M/L^3
Concentration, Polymer	c_p	M/L^3
Concentration, Solvent	c_s	M/L^3
Half Confinement Gap	B	L
Length, Center-to-Center Between Molecules	L	L
Length, Contour	L_c	L
Length, Persistence	L_p	L
Current Time	t	t
Frequency, Function of Confinement	ω_c	t^{-1}
Energy Values in Molecular-Scale Systems	kT	ML^2/t^2
Minus Imaginary Part of Nonlinear Complex Viscosity	η''	M/Lt
Molar Absorptivity	m_a	L^2/mole
Molecular Weight, Critical Entanglement	M_e	M/mole
Molecular Weight, Number-Average	M_n	M/mole
Molecular Weight, Weight-Average	M_w	M/mole
Number Density	n	$1/L^3$

Path Length of Sample	l_s	L
Real Part of Nonlinear Complex Viscosity	η'	M/Lt
Relaxation Time of Rigid Dumbbells	λ_0	t
Relaxation Time of Solution	λ	t
Residence Time	t_r	t
Shear Rate Amplitude	$\dot{\gamma}^0$	t^{-1}
Shear Rate Tensor	$\dot{\gamma}$	t^{-1}
Single-Harmonic Shear Stress Response	τ_{21}	M/Lt^2
Solvent Viscosity	η_s	M/Lt
Temperature	T	T
Velocity Gradient, Homogeneous Cosinusoidal	v_x	L/t
Velocity of Moving Plate	$v_0 \cos \omega t$	L/t
Velocity, Polymer migration	$v_{x,p}$	L/t
Velocity, Maximum	v_0	L/t
Velocity, Unconfined Bulk Flow	$v_{x,s}$	L/t
Viscosity, Infinite Shear Rate of Real Part	η_∞	M/Lt
Viscosity, Infinite Shear Rate of *Minus* Imaginary Part	η''_∞	M/Lt
Viscosity, Solvent	η_s	M/Lt
Viscosity, Zero-Shear of Real Part	η_0	M/Lt
Viscosity, Zero-Shear of *Minus* Imaginary Part	η''_0	M/Lt
Volumetric Flowrate, Polymer	q_p	L^3/t
Volumetric Flowrate, Solvent	q_s	L^3/t

Legend: $M \equiv$ mass; $L \equiv$ length; $t \equiv$ time

Table 2: Dimensionless Variables and Groups.

Name	Symbol	Range
Absorbance	A_{LB}	$0 \leq A_{LB} \leq 1$
Coefficient in Eqs. (35) and (36)	β	≥ 0
Concentration, Midplane	x_c	≥ 0
Concentration, Polymer	x_p	≥ 0
Concentration, Solvent	x_s	≥ 0
Confinement	L/B	≥ 0
Confinement Concentration Profile [see Eq. (61)]	χ_p	≥ 0
Confinement, Park and Fuller Definition	ε_f	$0 \leq \varepsilon_f \leq \infty$
Operator in Eq. (10) defined by Eq. (4) of [2]	Ω	
Operator in Eq. (10) defined by Eq. (5) of [2]	Λ	
Deborah Number, Oscillatory Shear	$\lambda\omega$	≥ 0
Entanglement Length	M_w/M_e	> 0
First Normal Stress Coefficient, from [2]	$\bar{b}_k(1)$	> 0
First Normal Stress Coefficient, from [112]	b_k	> 0
First Shear Stress Coefficient, from [2]	$\bar{a}_k(1)$	> 0
Probability Density for Internal Configuration of a Dumbbell	ψ	
Polar Angle	θ	
Polydispersity	M_w/M_n	> 0
Product of Weissenberg Number and Confinement	ε	≥ 0
Weissenberg Number	$Wi = \lambda\dot{\gamma}^0$	≥ 0

Chapter 1: Introduction

The greatest fascinations of chemical engineers with polymeric liquids are their curious behaviours when confined [1,2]. In this thesis, we use macromolecular theory, relying entirely on flow orientation, to explain the intriguing rheology of confined polymeric liquids (Chapter 2). Specifically, we use rigid dumbbell theory to explain the curious effects of polymer confinement: (a) diminishing complex viscosity (Chapter 2; [3]), and (b) emigration from high-shear (Chapter 3; [4,5]). From the latter, we arrive at the first completed fabrications of two confinement microfluidic separators (Chapter 4).

Table 3 classifies chronologically (with citations) the developing literature on polymer migration in microfluidics. Table 3 illustrates the novelty of each chapter (ex – Chapter 2; d – Chapter 3, f – for Chapter 4). The "Confinement Flow Type" column distinguishes concentration profiles arising in homogeneous or heterogeneous flow fields. By *homogeneous*, we mean constant shear rate through the gap. By *heterogeneous*, we mean otherwise.

Whereas much is known about the complex viscosity of polymeric liquids, far less is understood about the behaviour of this material function when macromolecules are confined. By *confined*, we mean that the gap along the velocity gradient is small enough to reorient the polymers. In the first part of this thesis, we examine classical analytical solutions [1] for a confined rigid dumbbell suspension in small-amplitude oscillatory shear flow. These analytical solutions are solutions to the diffusion equation [Eq. (15) of [6]; Eq. (10)] for a rigid dumbbell suspension subject to planar polymer orientation at the wall [Eq. (2) of [6]; Eq. (2) of [2]; Eqs. (11) and (12)] in oscillatory shear flow. The rigid dumbbell suspension is the simplest relevant model of a macromolecule whose reorientation is resisted by hydrodynamics. The rigid dumbbell has both length (center-

to-center distance, L) and width (bead diameter, d), where $L \geq d$. The beads are rigidly separated. We illustrate this with a dimensionless, massless rod, but the hydrodynamic resistance is captured by Stokes flow around the two dumbbell beads alone. The second dumbbell bead confers its orientation, since a single bead has none. We test these analytical solutions against the measured effects of confinement on both parts of the complex viscosity of a carbopol suspension (Figure 5 through Figure 8) and three polystyrene solutions (Figure 9, Figure 10, and Figure 11).

Microfluidic design, fabrication and experiments have developed rapidly, leading to lab-on-chip separation or fractionation [7,8]. In Chapter 3 of this thesis, we design a continuous concentrator for macromolecular solutions. Our design relies on the analytical solutions for orientational diffusion under laminar pressure-driven slot flow through a microchannel [5]. Using rigid dumbbell theory, we exploit prior theory [1] to arrive at new analytical solutions for the design of our microfluidic macromolecular hydrodynamic chromatography (Section 3.1 of Chapter 3). We arrive at our design through the use of well-known confinement-driven composition profiles [Eq. (42)]. Using a pair of razor-sharp blades, our design separates the slot flow into a symmetric core inner slot (concentrated) between two outer slots (diluted). We discover a minimum dimensionless blade leading edge separation for complete fractionation [Eq. (63) with Eqs. (44) and (62)], and that this decreases with confinement (Figure 14, Figure 15, and Figure 16), and also decreases with dimensionless shear rate.

Though much is known about particle sorting within microfluidic separators [7,9], far less is understood for polymer solutions. In Chapter 4, we design and fabricate two passive, continuous microfluidic separators. We do so using our earlier analytical rigid dumbbell theory for orientational diffusion under laminar pressure-driven slot flow

through a microchannel [5]. By *passive*, we mean channel geometry or particle inertia control the migration inside the microchannels [10]. We designed and fabricated (soft lithography) slot-flow (1,500 μm deep x 300 μm; Figure 19) and square duct (300 μm deep x 300 μm; Figure 20) straight microfluidic channels with one inlet and three outlets. We leave the measurements of the complex viscosity of this particular dilute polystyrene inlet solution and its concentrations at the three outlets for another day.

Our work on rigid dumbbell suspensions distinguishes itself from the more general rigid bead-rod theory (also called *rotarance* theory) [11,12,13,14,15] which would afford the exploration of the effects of macromolecular architecture on confinement. To our knowledge, nothing is known about the effects of macromolecular architecture on confinement. For this, we would begin by generalizing the foundational work on rigid dumbbells in confinement [1,5] to general rigid bead-rod theory.

Our work on rigid dumbbell suspensions confines itself to dilute systems. By *dilute,* we mean that the interactions between macromolecules are negligible relative to the hydrodynamic resistance to reorientation. Our use of the term *dilute* does not ensnare any other additional meaning (Chapter 9 of [16]).

Our work on rigid dumbbell suspensions further confines itself to systems where the interferences between the two Stokes flows are negligible relative to each Stokes flow itself. These interferences are called *intramolecular hydrodynamic interactions*, and these matter wherever L approaches d [17,18,19,20,21].

Although our work is mainly driven by curiosity, its applications have not escaped our attention (Chapter 4). The migration of polymer away from the walls is known to produce die lip buildup (also called *die drool*) in plastics extrusion [22,23,24,25,26,27].

The usefulness of the results of Chapter 3 for predicting die lip buildup in polymer extrusion is left for another day.

1.1. Timeline

For historical completeness, we diagram the timeline for this thesis research, updated from its plan (see Figure 13 of [28]). In pink, we highlight the research published extracurricular to this thesis [29,30,31,32].

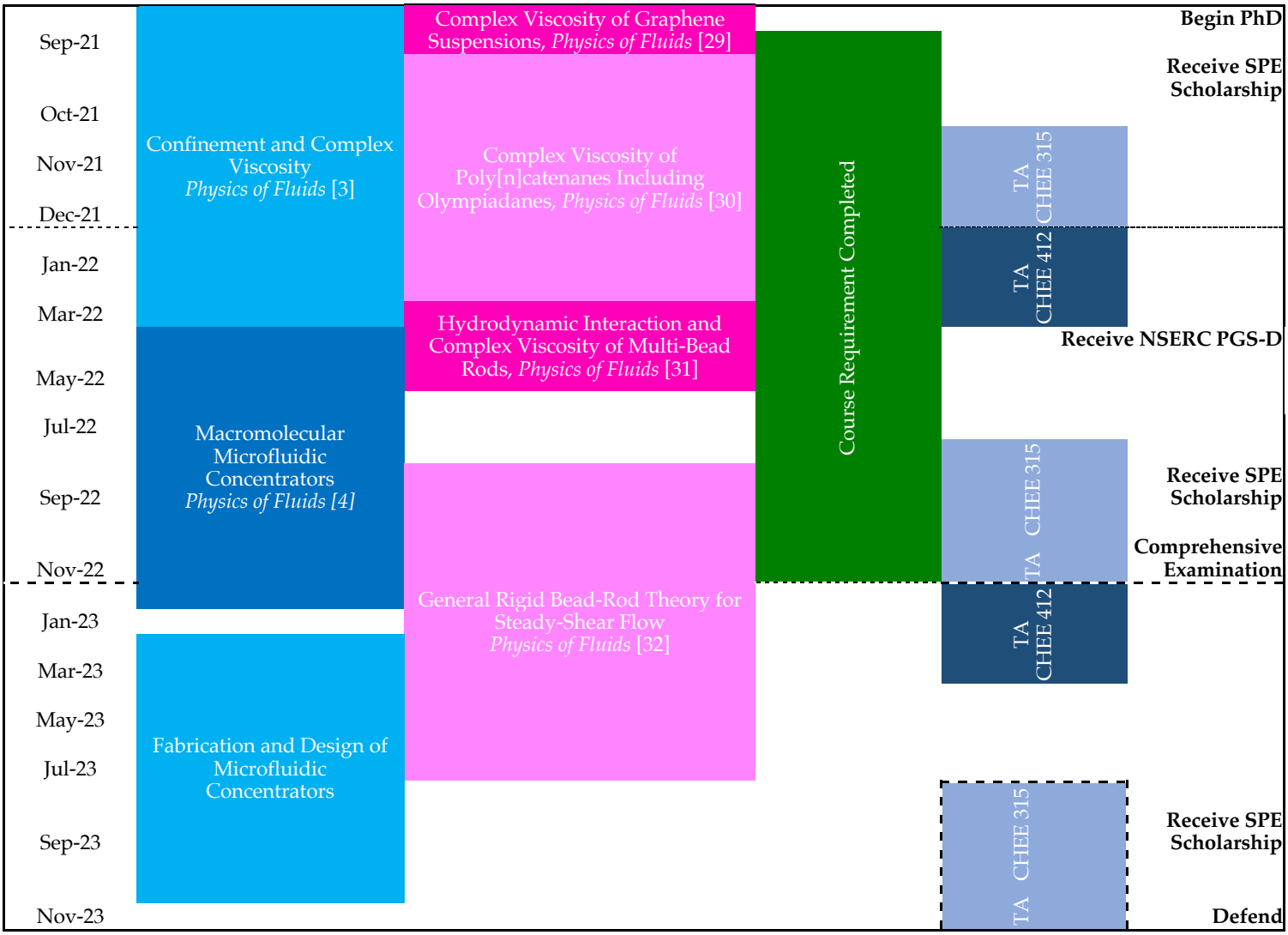

Figure 1: Timeline and progress for completion of PhD thesis and degree requirements.

1.2. Organization

We began by publishing substantially the contents of Chapter 2, and then of Chapter 3. Chapter 4 exploits the teachings of Chapter 3 to arrive at the completed fabrications of our two microfluidic concentrators. The subhead to this Introduction transports the reader into the confined flows by tying these chapters together (see Contents).

1.3. Objectives

In this work, we explore the (i) complex viscosity of polymer solutions in confinement in small-amplitude oscillatory shear flow (Chapter 2), and (ii) the lateral migration of these polymers in solution within microchannels (Chapters 3 and 4). For romanette (ii), we exploit the analytical solutions predicted by confined rigid dumbbell theory ([5]; Chapter 3). By *confined rigid dumbbell theory*, we at least mean to include complex viscosity of polymer solutions in microchannels (Chapter 2), concentration gradients of these polymer solutions across the microchannel (Chapter 3), and design and fabrication of these microfluidic devices (Chapter 4).

We establish a new subdiscipline of polymer migration from rigid dumbbell theory, which we call *rigid dumbbell migration*, and we apply this to polymer solutions. This work has resulted in 2 journal publications [3,4].

1.4. Contribution to Knowledge

We discover that (i) rigid dumbbell theory predicts confinement behaviours of polymer solutions (see Section 2.2.2; Figure 9, Figure 10, and Figure 11). We thus connect microfluidic confinement to the transport properties of polymer solutions.

We further discover (ii) that the persistence length of polymer orientation does not depend on concentration (Table 4).

We discover (iii) analytical solutions for microfluidic macromolecular separation (Chapter 3), where fractionation depends on channel gap and on the Weissenberg number for dilute polymer solutions.

Moreover, we discover that (iv) separation in polymer solution relying solely on orientational diffusion, lends itself to simple microfluidic designs (channel geometries) without the use of external forces (Chapter 4).

Table 3: Literature on polymer separation due to migration in microfluidics. Legend: a – analytical, d – design, n – numerical, s – simulation, ex – experimental, f – fabrication, PS – polymer solution, p – particles

Chapter		**Method**	**Confinement Flow Type**	**Fluid Type**	**Reference**
	Stasiak and Cohen (1983)	a	Heterogeneous	PS	[5]
	Park and Fuller (1985)	a	Homogeneous	PS	[1]
	Jendrejack *et al.* (2004)	s	Heterogeneous	PS	[33]
	Graham (2011)	ex, s	Heterogeneous	PS	[34]
	Sajeesh *et al.* (2013)	ex	Heterogeneous	p	[7]
	Rems *et al.* (2016)	ex, s	Heterogeneous	PS, p	[35]
	Alicia *et al.* (2017)	n, ex, s	Heterogeneous	p	[36]
2	Coombs *et al.* (2021)	a, ex	Homogeneous	PS	[3]
3	Coombs *et al.* (2022)	a, d	Heterogeneous	PS	[4]
4	Coombs (2023)	ex, f	Heterogeneous	PS	

Chapter 2: Confinement and Complex Viscosity

Reproduced from Coombs, S.J., R. Pasquino and A.J. Giacomin, "Confinement and Complex Viscosity," *Physics of Fluids*, **33**(4), 053104 (2021), pp. 1-7. Special Collection: Celebration of Robert Byron Bird (1924-2020). Editor's pick [3], with the permission of AIP Publishing.

One good way of explaining the elastic properties of liquids in the bulk is by considering their orientation distributions under flow [37,38,39,40]. Integrating these distributions in phase space yields the rheological properties (Section **IX.** of [6,41]). When the macromolecule is replaced by identical spheres of fixed center-to-center separation, L, we call its replacement a rigid dumbbell. We choose the rigid dumbbell suspension because it is the simplest relevant model macromolecule. By *relevant*, we mean that, at least qualitatively, it captures the observed behaviours for the most measured viscoelastic material functions [42,43].

In small-amplitude oscillatory shear flow, we subject the elastic liquid to the homogeneous cosinusoidal velocity gradient:

$$v_x(z,t) = v_0 \frac{z}{B} \cos \omega t \tag{1}$$

and thus a homogeneous cosinusoidal shear rate in simple shear flow (Eq. (26) of [44]):

$$\dot{\gamma} = \frac{v_0}{B} \equiv \dot{\gamma}^0 \cos \omega t \tag{2}$$

which nondimensionalizes as (Eq. (27) of [44]):

$$\dot{\lambda\gamma} \equiv \lambda \dot{\gamma}^0 \cos \lambda\omega(t/\lambda) \tag{3}$$

where λ is the fluid relaxation time, and where all symbols, dimensional and dimensionless are defined in Table 1 and Table 2. By *small-amplitude*, we normally mean (Eq. (29) of [44]):

$$\lambda \dot{\gamma}^0 < 1 \tag{4}$$

or its companion, from rigid dumbbell theory:

$$\lambda\dot{\gamma}^0 \ll \frac{1}{12\sqrt{2}} \tag{5}$$

We then measure the single-harmonic shear stress response (Eq. 4.4-3 of [45]):

$$\frac{\tau_{21}(t)}{\dot{\gamma}^0} \equiv [\eta'(\omega) + \eta_s]\cos\omega t + \eta''(\omega)\sin\omega t \tag{6}$$

where we define the complex viscosity as [46,47,48]:

$$\eta^* \equiv \eta' - i\eta'' \tag{7}$$

where η' is the real part, and η'', *minus* the imaginary. When the polymeric liquid touches the wall the macromolecules near the wall reorient (see Figure 2). So long as the gap is large, $B \gg L_p$, the measured η^* will be its bulk value and will just depend upon ω, and its orientation distribution will satisfy the diffusion equation (Eq. (15) of [6]):

$$6\lambda\frac{\partial\psi}{\partial t} = \Lambda\psi - 6\lambda\dot{\gamma}^0\cos\lambda\omega(t/\lambda)\,\Omega\psi \tag{8}$$

However, if the gap is not large, then η^* will depend upon both ω and the macromolecular confinement [5]:

$$\varepsilon_f \equiv \frac{L_p}{B} \tag{9}$$

and the orientation distribution will depend on z and depart from Eq. (8) as follows (combining Eq. (8) with Eq. (1) of [2]):

$$6\lambda\frac{\partial\psi}{\partial t} = \Lambda\psi - 6\lambda\dot{\gamma}^0\cos\lambda\omega(t/\lambda)\,\Omega\psi - \tfrac{1}{4}\varepsilon_f^2\frac{\partial^2\psi}{\partial z^2} \tag{10}$$

where (Eq. (2) of [6]):

$$-\frac{1}{\sin\theta}\frac{\partial\psi}{\partial\theta} \pm \varepsilon_f\frac{\partial\psi}{\partial z} = 0 \tag{11}$$

at (Eq. (2) of [2]):

$$z = \frac{1}{2}\left(1 \pm \varepsilon_f \cos\theta\right) \tag{12}$$

Eqs. (10) through (12) thus define how confinement affects macromolecular orientation in small-amplitude oscillatory shear flow of rigid dumbbell suspensions. Whereas in Eq. (9), Park and Fuller interpret the persistence length of macromolecular confinement, L_p, as L (after Eq. (3) of [2]), Stasiak and Cohen interpret L_p as $2\lambda\dot{\gamma}^0 L$ [5] (Chapter 3). In this paper, we shall measure L_p.

The well-known expressions for the parts of the bulk complex viscosity are (Eq. (8) of [6]):

$$\frac{\eta'(\omega) - \eta_s}{nkT\lambda} = 1 - \frac{3}{5}\frac{(\lambda\omega)^2}{1 + (\lambda\omega)^2} = \frac{1}{1 + (\lambda\omega)^2}\left(1 + \frac{2}{5}(\lambda\omega)^2\right) \tag{13}$$

and:

$$\frac{\eta''(\omega)}{nkT\lambda} = \frac{3\lambda\omega}{5(1 + (\lambda\omega)^2)} \tag{14}$$

where, in the limits as $\lambda\omega \to 0$, we get:

$$\frac{\eta_0 - \eta_s}{nkT\lambda} = 1 \tag{15}$$

and:

$$\frac{\eta_0''}{nkT\lambda} = 0 \tag{16}$$

where, in the limits as $\lambda\omega \to \infty$, we get:

$$\frac{\eta_\infty - \eta_s}{nkT\lambda} = \frac{2}{5} \tag{17}$$

and:

$$\frac{\eta_\infty''}{nkT\lambda} = 0 \tag{18}$$

and, for the rigid dumbbell (Eq. (6) of [6]):

$$\lambda \equiv \frac{\xi L^2}{12kT} \equiv \frac{\pi d \eta_s L^2}{4kT} \tag{19}$$

which is well-known. For an osculated dumbbell:

$$\lambda \equiv \frac{\xi L^2}{12kT} \equiv \frac{\pi \eta_s L^3}{4kT} \tag{20}$$

so that:

$$L = \sqrt[3]{\frac{4kT\lambda}{\pi \eta_s}} \tag{21}$$

which we will use below.

One of the great challenges in microfluidics is understanding the fluid microstructure near its confining walls [49,50,51]. To deepen this understanding experimentally we turn to thin-film rheology, where rheological material functions are measured as functions of confinement (by varying the gap). In this research, we turn our attention specifically to the complex viscosity measured as a function of confinement [52,1].

2.1. Confinement Method

As the gap decreases, and thus the macromolecular confinement increases, the wall reorientations begin to decrease the measured value of η' by an amount that depends on the confinement. For the rigid dumbbell suspension, the well-known results for the parts of the confined complex viscosity for small confinement, when $0 \leq \varepsilon_f \leq 1$ (Eqs. (2-57a) and (2-57b) of [52]):

$$\frac{\eta'(\omega, \varepsilon_f) - \eta_s}{nkT\lambda} = \frac{1}{1 + (\lambda\omega)^2} \left\{ \frac{1 - \varepsilon_f}{1 - \frac{\varepsilon_f}{2}} \left(1 + \frac{2}{5} (\lambda\omega)^2 \right) + \frac{\frac{\varepsilon_f}{2}}{1 - \frac{\varepsilon_f}{2}} \left(\frac{1}{2} + \frac{1}{20} (\lambda\omega)^2 \right) \right\} \tag{22}$$

and:

$$\frac{\eta''(\omega,\varepsilon_f)}{nkT\lambda}=\frac{3\lambda\omega}{5(1+(\lambda\omega)^2)}\left\{\frac{1-\frac{5\varepsilon_f}{8}}{1-\frac{\varepsilon_f}{2}}\right\} \tag{23}$$

which expand as:

$$\frac{\eta'(\omega,\varepsilon_f)-\eta_s}{nkT\lambda}=\frac{1}{1+(\lambda\omega)^2}\left\{1-\frac{\varepsilon_f}{4}+\frac{11\varepsilon_f^2}{40}-\frac{19\varepsilon_f^3}{80}-\cdots\right\} \tag{24}$$

and:

$$\frac{\eta''(\omega,\varepsilon_f)}{nkT\lambda}=\frac{3\lambda\omega}{5(1+(\lambda\omega)^2)}\left\{1-\frac{\varepsilon_f}{8}-\frac{\varepsilon_f^2}{16}-\frac{\varepsilon_f^3}{32}-\cdots\right\} \tag{25}$$

where, in the limits as $\lambda\omega\to 0$, we get:

$$\frac{\eta_0-\eta_s}{nkT\lambda}=\frac{1-\frac{3\varepsilon_f}{4}}{1-\frac{\varepsilon_f}{2}}=1-\frac{\varepsilon_f}{4\left(1-\frac{\varepsilon_f}{2}\right)}=1-\frac{1}{4}\varepsilon_f-\frac{1}{8}\varepsilon_f^2-\cdots \tag{26}$$

and:

$$\frac{\eta_0''}{nkT\lambda}=0 \tag{27}$$

from which we learn that the zero-shear value of η'' is unaffected by confinement. From Eqs. (22) and (23), we learn that rigid dumbbell confinement theory predicts the fitted value of L_p to be independent of both $\lambda\omega$ and $\lambda\dot{\gamma}^0$. From Eq. (26), we learn that the polymer contribution to the zero-shear viscosity descends with confinement, and that as confinement decreases, its unconfined value is not approached asymptotically. Eq. (26) agrees with Eq. (25) of [1] for its special case of zero-shear, where $f(t)=(1;t)=1$, as it must. Eq. (26) also agrees with Eq. (25b) of [2], and with Eq. (38a) of [2] for its special case of zero-shear, as it must. In the limit of vanishing confinement, as $\varepsilon_f\to 0$, Eqs. (22) and (23) reduce to the well-known expressions for the bulk complex viscosity, Eqs. (13) and (14), as they must. Further, in the limit of vanishing confinement, Eqs. (26) and (27)

reduce to the well-known expressions for the bulk zero-shear viscosity and η_0'', Eqs. (15) and (16), as they must.

For large confinement, when $\varepsilon_f \geq 1$ (Eqs. (2-58a) and (2-58b) of [52]):

$$\frac{\eta'(\omega,\varepsilon_f)-\eta_s}{nkT\lambda}=\frac{1}{1+(\lambda\omega)^2}\left\{\frac{1}{2\varepsilon_f^2}+\left[-\frac{1}{4\varepsilon_f^2}+\frac{3}{10\varepsilon_f^4}\right](\lambda\omega)^2\right\} \tag{28}$$

and:

$$\frac{\eta''(\omega,\varepsilon_f)}{nkT\lambda}=\frac{3\lambda\omega}{5(1+(\lambda\omega)^2)}\left\{\frac{5}{4\varepsilon_f^2}\left[1-\frac{2}{5\varepsilon_f^2}\right]\right\} \tag{29}$$

which are the counterparts to Eqs. (22) and (23).

Nondimensionalizing and normalizing Eqs. (22) and (23) with Eq. (26) yields, for $0 \leq \varepsilon_f \leq 1$:

$$\frac{\eta'-\eta_s}{\eta_0-\eta_s}=\frac{(15\varepsilon_f-16)(\lambda\omega)^2+30\varepsilon_f-40}{(30\varepsilon_f-40)(\lambda\omega)^2+30\varepsilon_f-40}=\frac{(15\varepsilon_f-16)(\lambda\omega)^2+30\varepsilon_f-40}{30(1+(\lambda\omega)^2)\left(\varepsilon_f-\frac{4\varepsilon_f}{3}\right)} \tag{30}$$

and:

$$\frac{\eta''}{\eta_0-\eta_s}=\frac{3\lambda\omega}{5(1+(\lambda\omega)^2)}\left\{\frac{1-\frac{5\varepsilon_f}{8}}{1-\frac{3\varepsilon_f}{4}}\right\}=\frac{3\lambda\omega(5\varepsilon_f-8)}{10(1+(\lambda\omega)^2)(3\varepsilon_f-4)} \tag{31}$$

which, in the limit of vanishing confinement, give the bulk values:

$$\frac{\eta'-\eta_s}{\eta_0-\eta_s}=\frac{1+\frac{2}{5}(\lambda\omega)^2}{1+(\lambda\omega)^2} \tag{32}$$

and:

$$\frac{\eta''}{\eta_0-\eta_s}=\frac{3}{5}\frac{\lambda\omega}{(1+(\lambda\omega)^2)} \tag{33}$$

whose counterparts are Eqs. (22) and (23). In this paper, we will use Eqs. (22) and (23) to deepen our understanding of confinement, and Eqs. (32) and (33) to compare with the available confined complex viscosity measurements.

Examining Eq. (9), we see that experimental measurements of confinement can be arrived at by varying either the orientation persistence length, L_p [53,54,55], or by varying the gap, B. However, increasing L_p confounds increases in both bulk properties, λ and η_0, with confinement. For evaluating theory, such as Eqs. (22) and (23) [or their companions, Eqs. (30) and (31)] we thus much prefer varying the gap, B (Fig. 9 of [56], Fig. 11 of [57]).

2.2. Confinement Results

Plotted from Eqs. (22) and (28), Figure 3 shows that, for a suspension of rigid dumbbells, confinement decreases the real part of the complex viscosity at all frequencies. From Eq. (23) and (29), Figure 4 shows likewise for *minus* the imaginary part. Examining the left side of Figure 3, we see that the zero-shear viscosity decreases with confinement, as Eq. (26) predicts. Examining Eq. (22), we see that we can measure the confinement persistence length L_p by fitting Eq. (22) to $\eta'(\omega, \varepsilon_f)$ measurements. We shall do so presently.

2.2.1. Worked Example: Carbopol

We next test Eq. (22) against experimental measurements of $\eta'(\omega, \varepsilon_f)$ for a neutralized aqueous 0.15 weight percent Carbopol suspension at room temperature. Whereas Carbopol particles are less than 10 microns across (Fig. 12 of [57]), their much larger flocculated structure is the relevant orienting body causing the complex viscosity. Figure 5 (or on log scales, Figure 6) shows that for the flocculated Carbopol suspension,

rigid dumbbell theory describes adequately the real part of the complex viscosity $\lambda\omega < 5$. Less adequately, as Figure 7 (or on log scales, Figure 8) shows, does rigid dumbbell theory describe *minus* the imaginary part of the complex viscosity. For the latter, we find qualitative agreement, but not quantitative.

From the lower curve in Figure 5 we learn that Eq. (28) fits the confinement measurements for the value $\varepsilon_f = 0.60$. From Eq. (9) we then discover that for the flocculated Carbopol structures, viewed through the lens of rigid dumbbell theory, $L_p = 0.60(145\ \mu\text{m}) = 87\ \mu\text{m}$.

2.2.2. Worked Example: Atactic Polystyrene

Rheological experiments were performed at $T = 24℃$ with the strain-controlled rheometer ARES (TA Instrument), using a 25mm parallel disk geometry, at variable gap. We characterized our nearly monodisperse atactic polystyrene, for which $M_w = 200{,}000$ g/gmol [degree of polymerization 1921, $c^* \cong 0.01$ g/ml] and $M_w/M_n = 1.01$, dissolved in diethylphthalate at three concentrations in small-amplitude oscillatory shear flow generated between parallel disks. This polystyrene has been studied previously [58], though not in solution. Since the entanglement molecular weight of polystyrene is $M_e = 18{,}100$ g/gmol, each polystyrene chain is 11 entanglement lengths, that is, $M_w/M_e = 11$. Table 4 lists the concentrations of the semi-dilute, threshold, and concentrated polystyrene solutions that we have studied. To define *semi-dilute*, *threshold*, and *concentrated*, we rely on Figure 1 of [59]. All complex viscosity measurements were made at a shear strain amplitude of 0.30, where $\dot{\gamma}^0$ is evaluated at the disk rim, producing Weissenberg numbers in excess of those given by Eqs. (4) and (5) (see Table 4). For all three polystyrene solutions of this subsection, no nonlinearity is observed up

to shear strain amplitudes of 0.50. The viscosity of diethylphthalate at $T = 24℃$ is $\eta_s = 0.086$ Pa s [60].

In Section 2.2.1., we began with a set of $\eta'(\omega, \varepsilon_f)$ curves, then fitted λ and η_0 of Eq. (13) to the measured bulk $\eta'(\omega, 0)$ curve. By contrast, for the atactic polystyrene solution examples to follow, we proceed from the complex viscosity measured at a single frequency, as a function of confinement, $\eta'(\omega_c, \varepsilon_f)$. Evaluating Eq. (24) at zero confinement yields, from the intercept, the quadratic:

$$(\lambda\omega_c)^2 - \frac{nkT}{(\eta'(\omega_c, \varepsilon_f) - \eta_s)\omega_c}\lambda\omega_c + 1 = 0 \tag{34}$$

so that:

$$\lambda\omega_c = \frac{\beta \pm \sqrt{\beta^2 - 4}}{2} \tag{35}$$

where:

$$\beta \equiv \frac{nkT}{(\eta'(\omega_c, \varepsilon_f) - \eta_s)\omega_c} \tag{36}$$

yielding:

$$\lambda\omega_c = \frac{1}{2}\frac{nkT}{(\eta'(\omega_c, \varepsilon_f) - \eta_s)\omega_c} - \frac{1}{2}\sqrt{\left(\frac{nkT}{(\eta'(\omega_c, \varepsilon_f) - \eta_s)\omega_c}\right)^2 - 4} \tag{37}$$

which we will use to get λ for each solution, and then fit L_p to the measured $\eta'(\omega_c, \varepsilon_f)$ curve for each solution.

We next proceed with our new complex viscosity confinement measurements on three concentrations of the atactic polystyrene solution, chosen for their three different states of entanglement: semi-dilute ($cM_w/c^* = 10 \times 10^9$ g/L), threshold ($cM_w/c^* = 20 \times 10^9$ g/L), and concentrated ($cM_w/c^* = 30 \times 10^9$ g/L). For the semi-dilute solution,

Figure 9 compares rigid dumbbell confinement theory, Eq. (22), with the measured real part of the complex viscosity versus dimensionless confinement. We find good agreement in that (1) η' descends with ε_f, and (2) that the initial slope is nonzero, negative, and specifically:

$$\left.\frac{d\eta'}{d\varepsilon_f}\right|_{\varepsilon_f \to 0} \cong -\frac{1}{4} \tag{38}$$

that is, the coefficient of the first order term in the expansion, Eq. (24). For the threshold solution, Figure 10 compares the confinement theory, Eq. (22), with the measurements. We again find good agreement: (1) η' descends with ε, and (2) Eq. (38) is confirmed. For the concentrated solution, Figure 11 tests confinement theory, Eq. (22), against the measurements. Again, for the concentrated solution, (1) η' descends with ε_f, and (2) Eq. (38) is confirmed.

Table 4 lists the fitted values of λ, η_0, and L_p for the three polystyrene solutions of this subsection. Both λ and η_0 increase with concentration. From Table 4, we find that the fitted orientation persistence length, L_p, does not depend on concentration. This suggests that the interactions between neighbouring macromolecules hardly matter compared to the hydrodynamic resistance to the reorientation (see Subhead to Introduction). We find the L_p fitted to the confinement experiments to be much larger than the rigid polystyrene chain contour length ($L_c = 860$ nm):

$$\frac{L_p}{L_c} \cong 150 \tag{39}$$

The value of L_p fitted to the confinement experiments for the polystyrene solutions of 0.13 mm is not too far from the value fitted for the carbopol suspension of 0.087 mm (of

Section 2.2.1 above). From Table 4, we also find that the center-to-center dumbbell length, L, calculated from Eq. (21) increases with concentration.

For the semi-dilute and threshold polystyrene solutions, we find that:

$$\frac{\eta''(\omega_c, \varepsilon_f)}{\eta'(\omega_c, \varepsilon_f)} \ll 1 \tag{40}$$

Our measurements thus produced no useful tests of Eq. (23). However, Eq. (40) was not obtained for our concentrated polystyrene solution measurements. Figure 12 tests Eq. (23) for the effect of confinement on the fluid elasticity against our concentrated polystyrene solution measurements. We find good agreement in that (1) η'' descends with ε, and (2) that the initial slope is nonzero, negative, and specifically:

$$\left.\frac{d\eta''}{d\varepsilon_f}\right|_{\varepsilon_f \to 0} \cong -\frac{1}{8} \tag{41}$$

that is, the coefficient of the first order term in the expansion, Eq. (25). However, as was the case for the Carbopol agglomerate suspension (Section 2.2.1 above), Eq. (23) overpredicts η'', in this case, by a factor of 2.

Rigid dumbbell confinement theory, Eqs. (22) and (23), predicts the fitted value of L_p to be independent of $\lambda\omega$ and $\lambda\dot{\gamma}^0$. Table 4 lists the ranges of $\lambda\omega$ and $\lambda\dot{\gamma}^0$ over which our oscillatory shear flow experiments were taken. Table 4 shows that L_p does indeed appear to be independent of the $\lambda\omega$ and $\lambda\dot{\gamma}^0$.

Table 4: Polystyrene Solution Results

c, mg/mL	ω_c, rad/s	$\dot{\gamma}^0$, s^{-1}	nkT, Pa	λ, s	η_0, Pa s	L, mm Eq. (21)	$\lambda\omega_c$	$\lambda\dot{\gamma}^0$	L_p, mm
0.050	50.1	15.0	0.617	0.34	0.21	2.74×10^{-7}	17.03	5.10	0.13
0.10	50.1	15.0	1.235	0.65	0.80	3.41×10^{-7}	32.57	9.75	0.13
0.15	31.6	9.5	1.852	1.00	1.85	3.93×10^{-7}	31.60	9.50	0.13

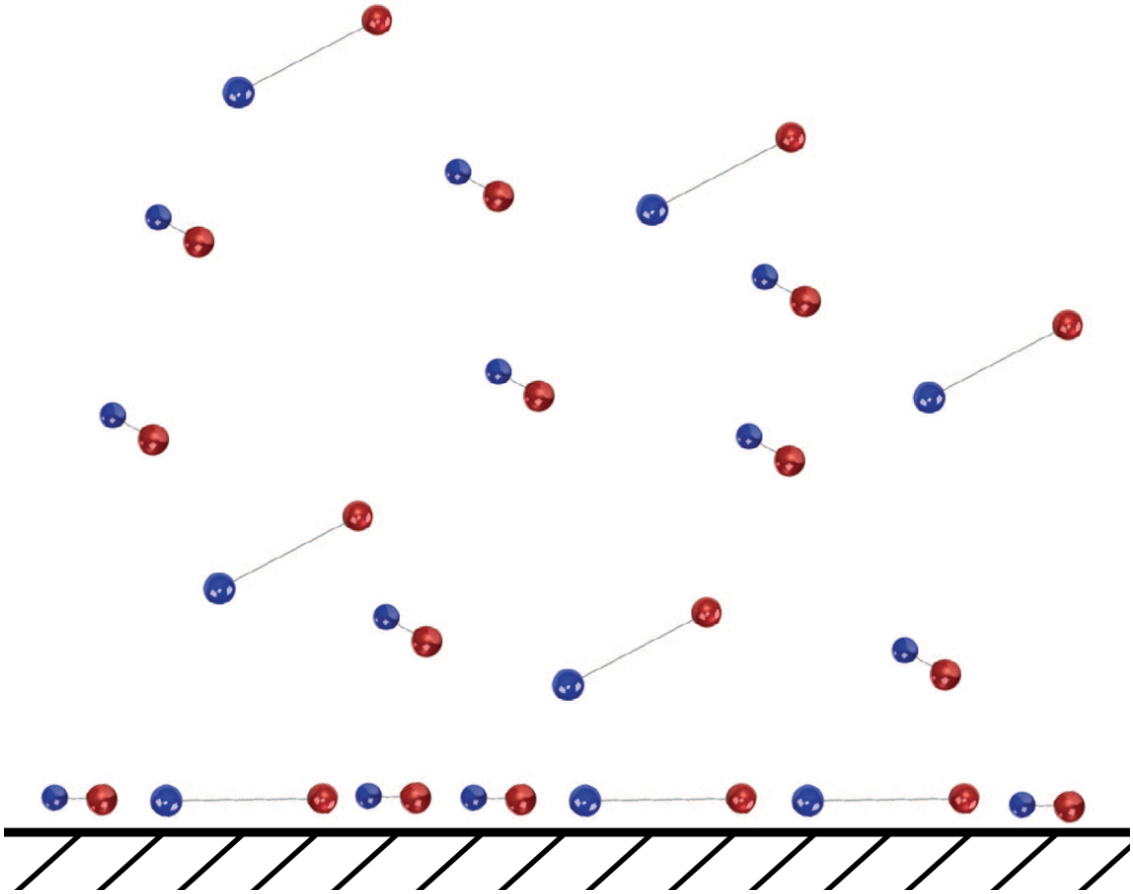

Figure 2: Macromolecular reorientation near wall for fluid at rest.

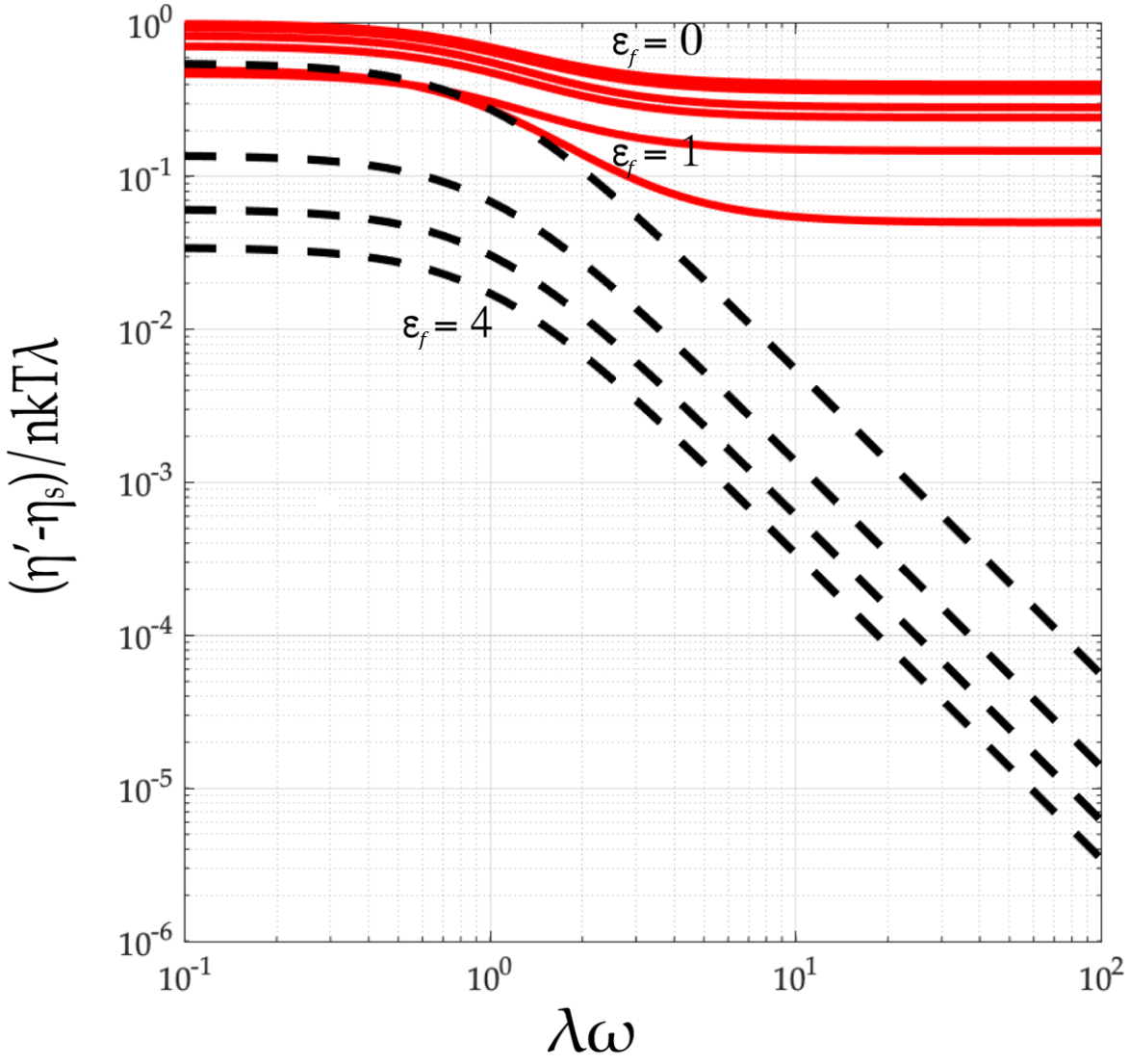

Figure 3: Universal dimensionless plots for η' vs $\lambda\omega$ at varying confinement [Eqs. (22) (**red**) and (28) (**black**)].

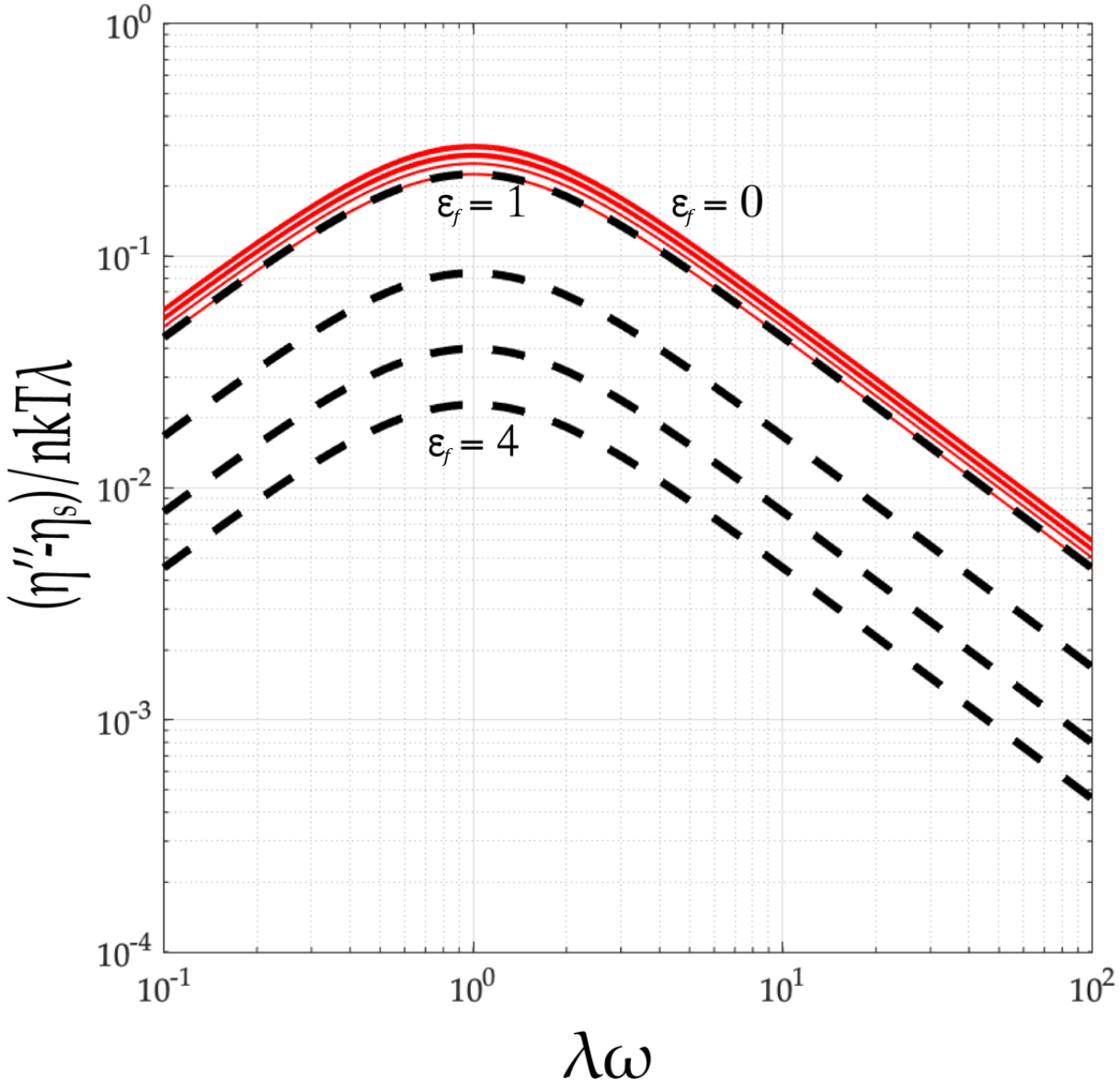

Figure 4: Universal dimensionless plots for η'' vs $\lambda\omega$ at varying confinement [Eq. (23) (**red**) and (29) (**black**)].

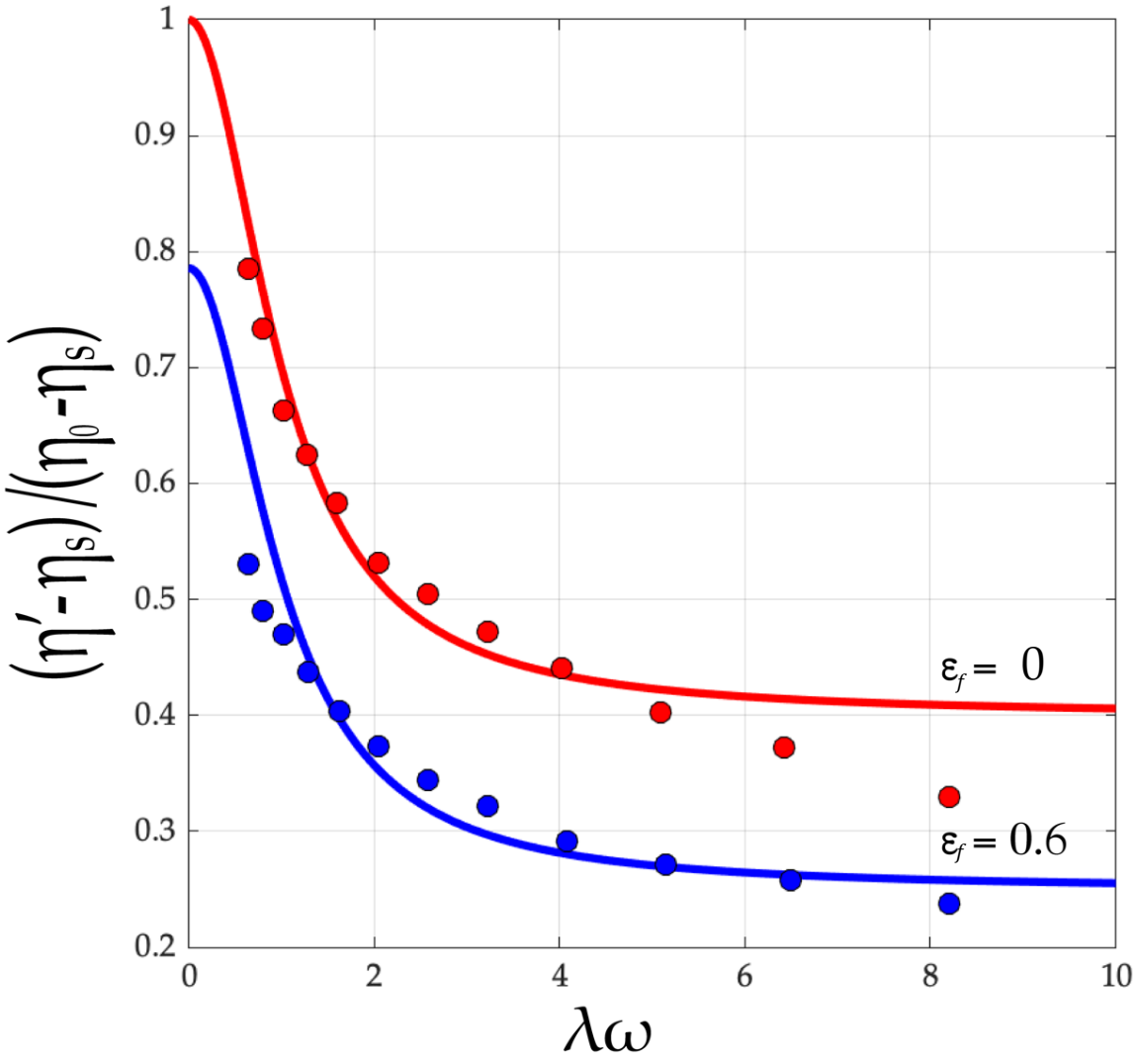

Figure 5: Upper curve (**red**) is Eq. (30) fitted to $\eta'(\omega)$ measurements of aqueous Carbopol suspension at $B = 199\ \mu$m (hollow circles in Fig. 11(a) of [57]) with $\lambda = 1.3$ s and $\eta_0 = 1.0$ Pa · s. Lower curve (**blue**) is Eq. (28) fitted to $\eta'(\omega, \varepsilon_f)$ measurements at $B = 145\ \mu$m (hollow inverted triangles in Fig. 11(a) of [57]) with $\lambda = 1.3$ s, $\eta_0 = 1.0$ Pa · s, and $\varepsilon_f = 0.60$.

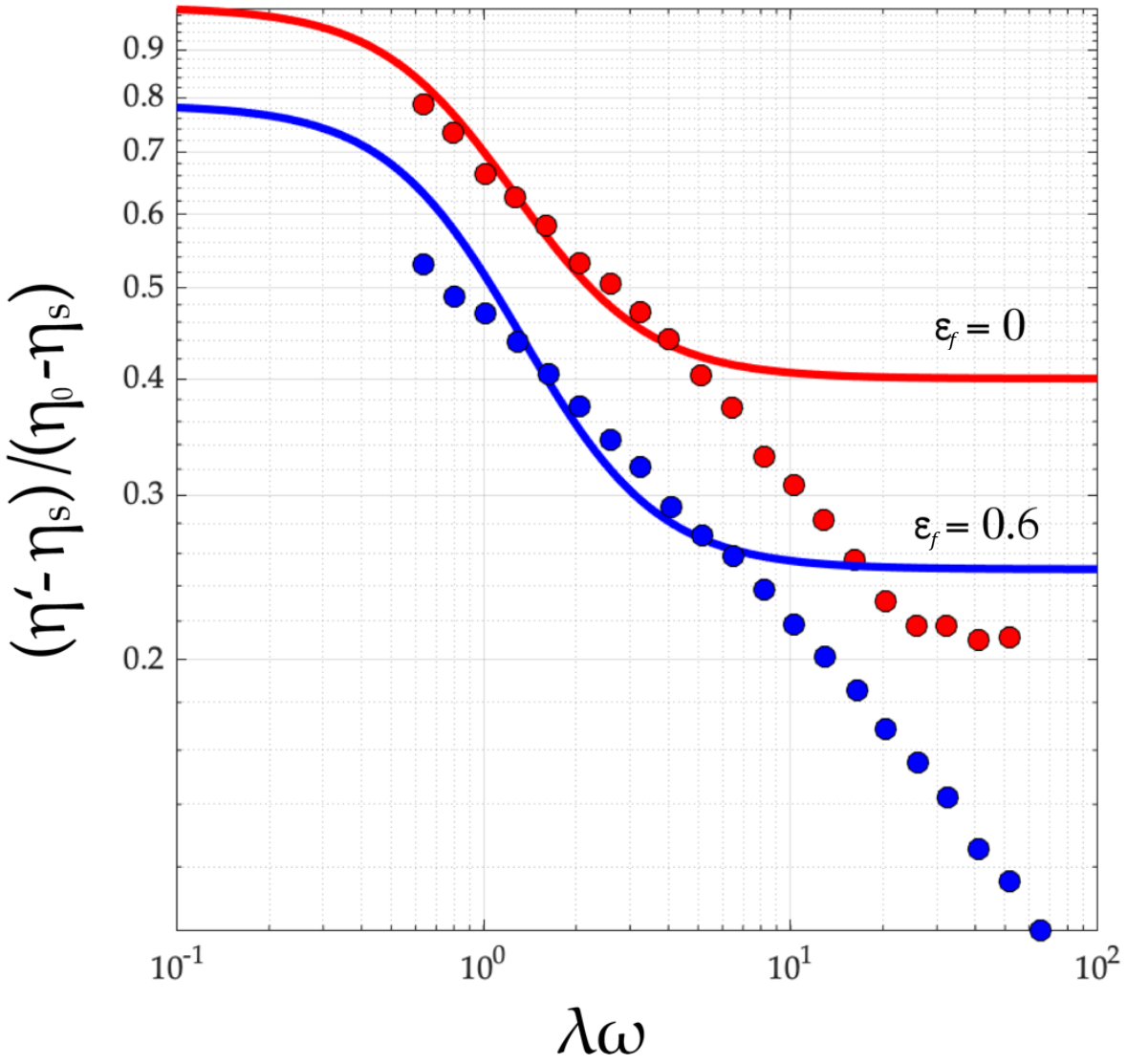

Figure 6: Upper curve (**red**) is Eq. (30) fitted to $\eta'(\omega)$ measurements of aqueous Carbopol suspension at $B = 199\ \mu$m (hollow circles in Fig. 11(a) of [57]) with $\lambda = 1.3$ s and $\eta_0 = 1.0$ Pa · s. Lower curve (**blue**) is Eq. (28) fitted to $\eta'(\omega, \varepsilon_f)$ measurements at $B = 145\ \mu$m (hollow inverted triangles in Fig. 11(a) of [57]) with $\lambda = 1.3$ s, $\eta_0 = 1.0$ Pa · s, and $\varepsilon_f = 0.60$.

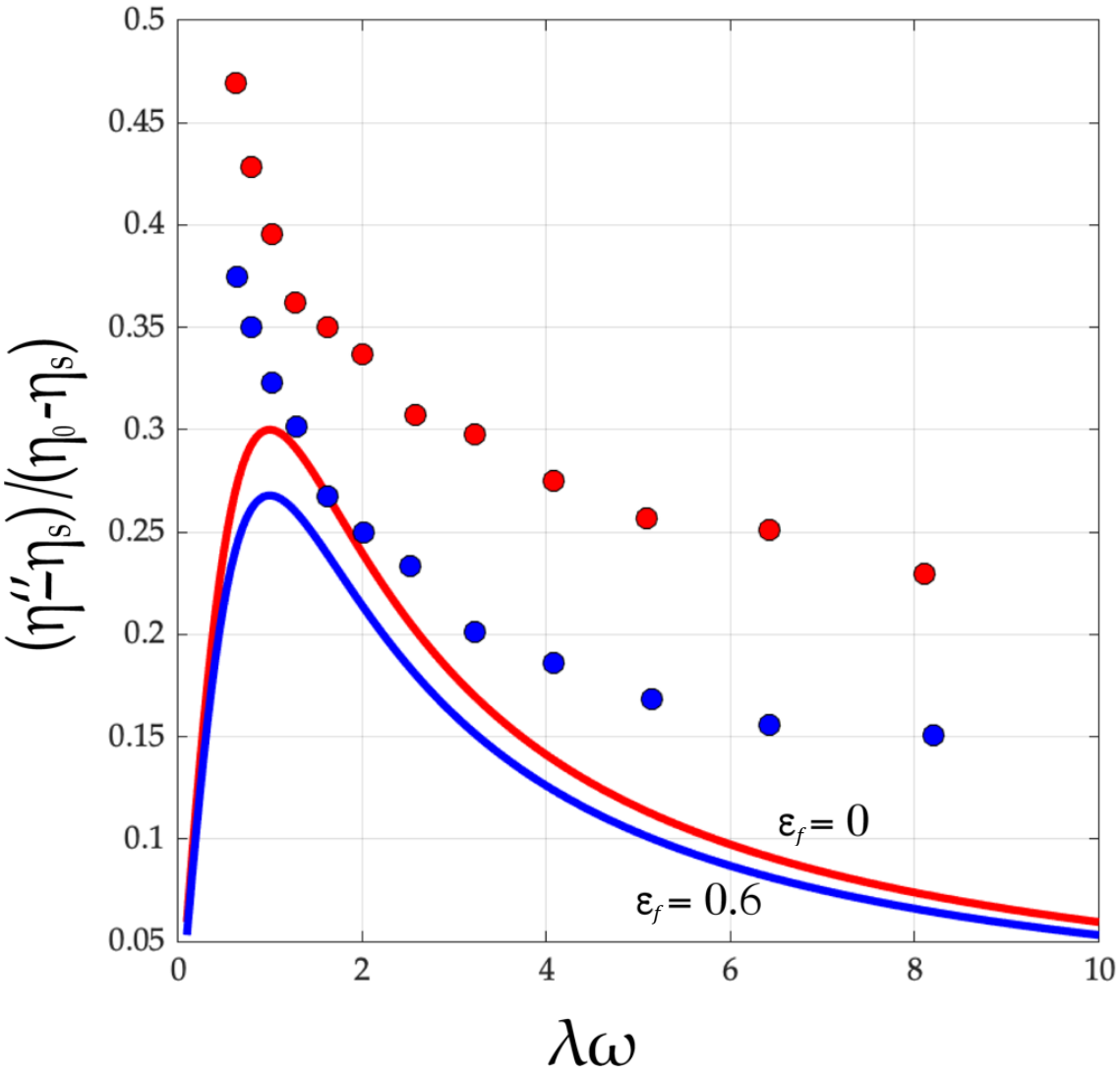

Figure 7: Upper curve is Eq. (31) fitted to $\eta''(\omega)$ measurements of aqueous Carbopol suspension at $B = 199\ \mu$m (solid circles in Fig. 11(a) of [57]) with $\lambda = 1.3$ s and $\eta_0 = 1.0\ \text{Pa} \cdot \text{s}$. Lower curve is Eq. (29) fitted to $\eta''(\omega, \varepsilon_f)$ measurements at $B = 145\ \mu$m (solid inverted triangles in Fig. 11(a) of [57]) with $\lambda = 1.3$ s, $\eta_0 = 1.0\ \text{Pa} \cdot \text{s}$, and $\varepsilon_f = 0.60$.

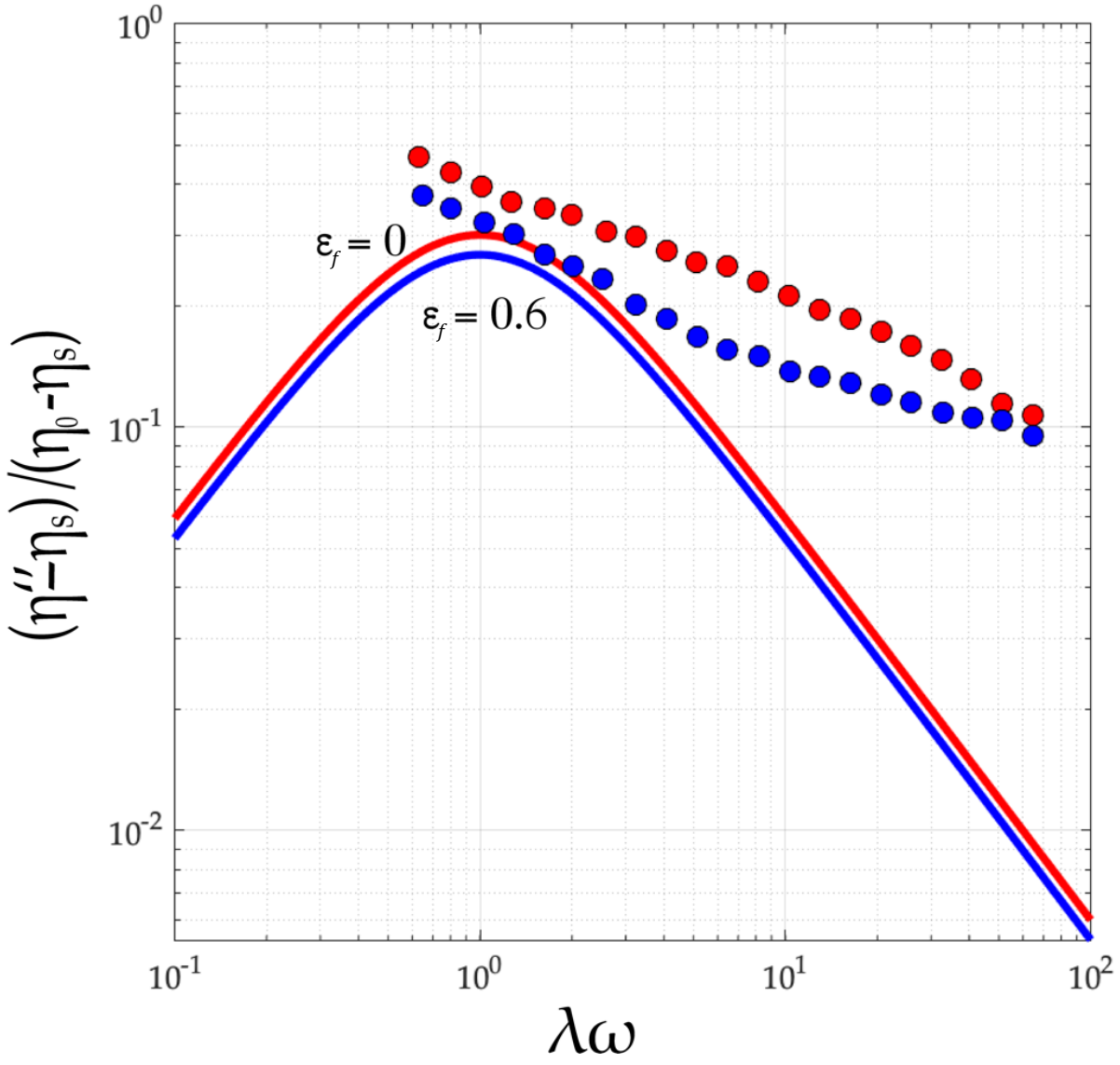

Figure 8: Upper curve (**red**) is Eq. (31) fitted to $\eta''(\omega)$ measurements of aqueous Carbopol suspension at $B = 199\ \mu$m (solid circles in Fig. 11(a) of [57]) with $\lambda = 1.3$ s and $\eta_0 = 1.0$ Pa $\cdot$ s. Lower curve (**blue**) is Eq. (29) fitted to $\eta''(\omega, \varepsilon_f)$ measurements at $B = 145\ \mu$m (solid inverted triangles in Fig. 11(a) of [57]) with $\lambda = 1.3$ s, $\eta_0 = 1.0$ Pa $\cdot$ s, and $\varepsilon_f = 0.60$.

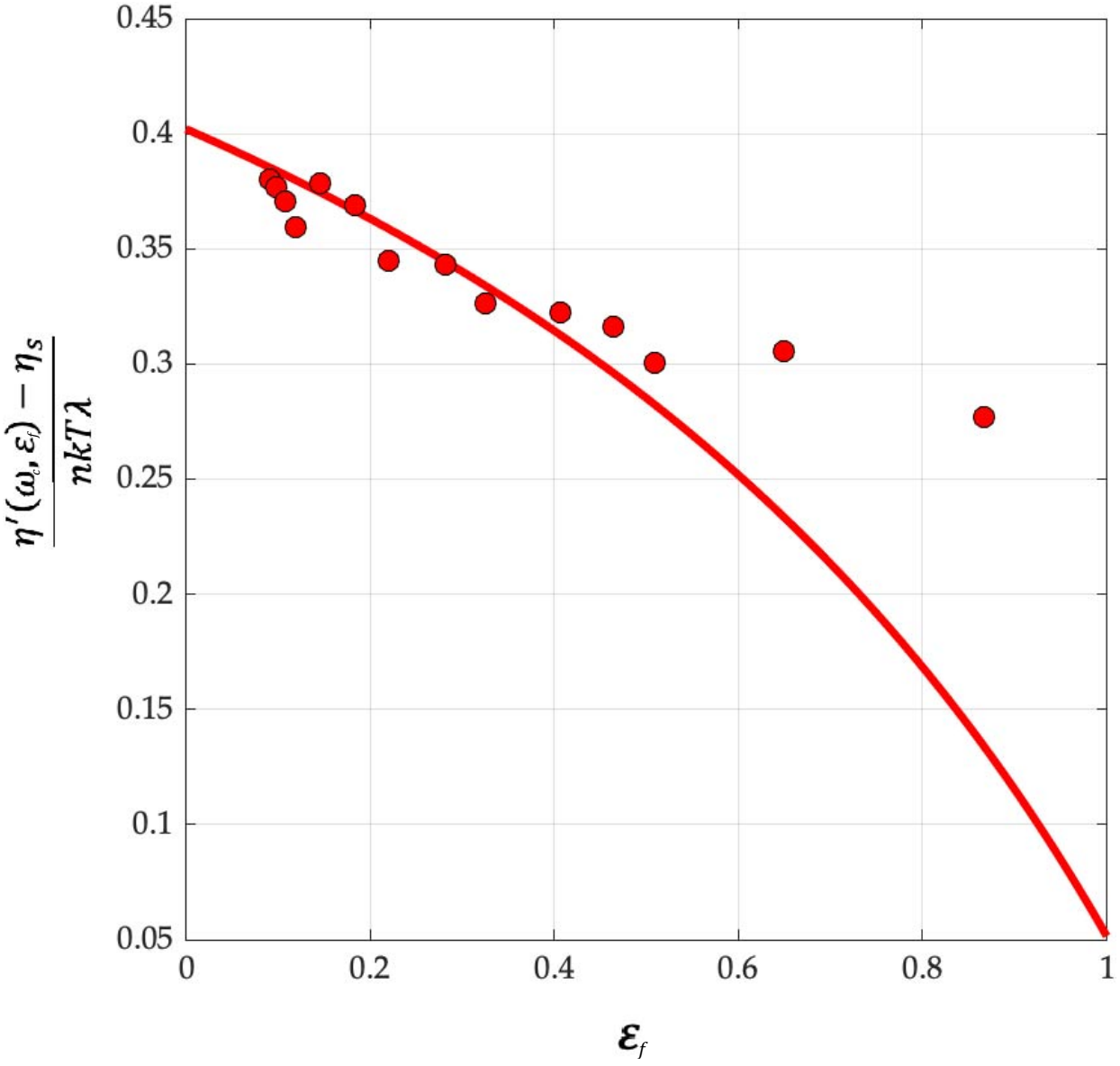

Figure 9: Eq. (22) fitted to $\eta'(\omega_c, \varepsilon_f)$ measurements of polystyrene in diethylphthalate at $c = 0.05$ mg/mL with $nkT = 0.617$ Pa, $T = 24$°C and $\omega_c = 50.1$ rad/s, with $\lambda = 0.34$ s and $L = 0.13$ mm. Semi-dilute; $cM_w/c^* = 10 \times 10^9$ g/L.

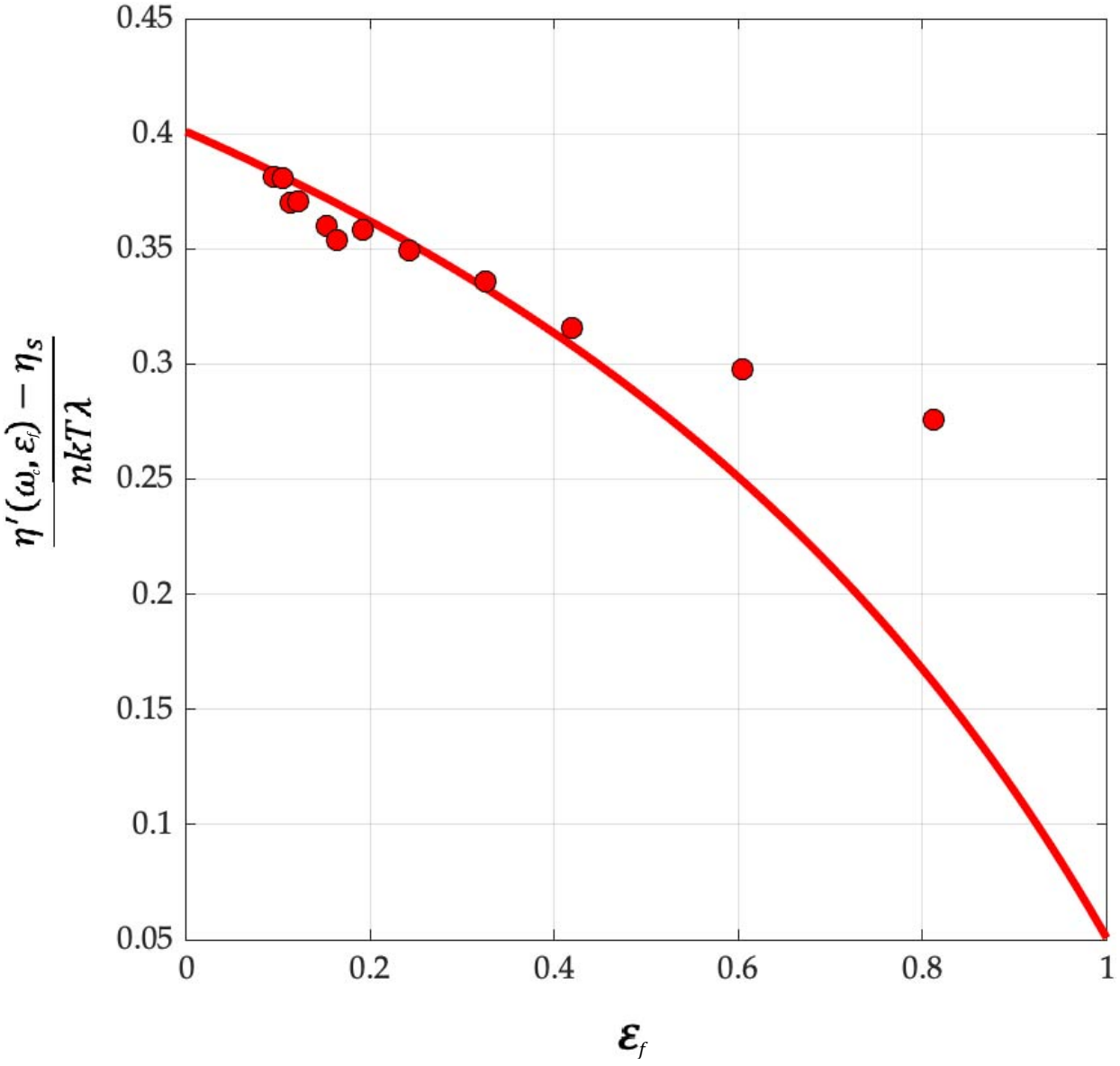

Figure 10: Eq. (22) fitted to $\eta'(\omega_c, \varepsilon_f)$ measurements of polystyrene in diethylphthalate at $c = 0.1$ mg/mL with $nkT = 1.235$ Pa, $T = 24$℃ and $\omega_c = 50.1$ rad/s, with $\lambda = 0.65$ s and $L = 0.13$ mm. Between semi-dilute and entangled; $cM_w/c^* = 20 \times 10^9$ g/L.

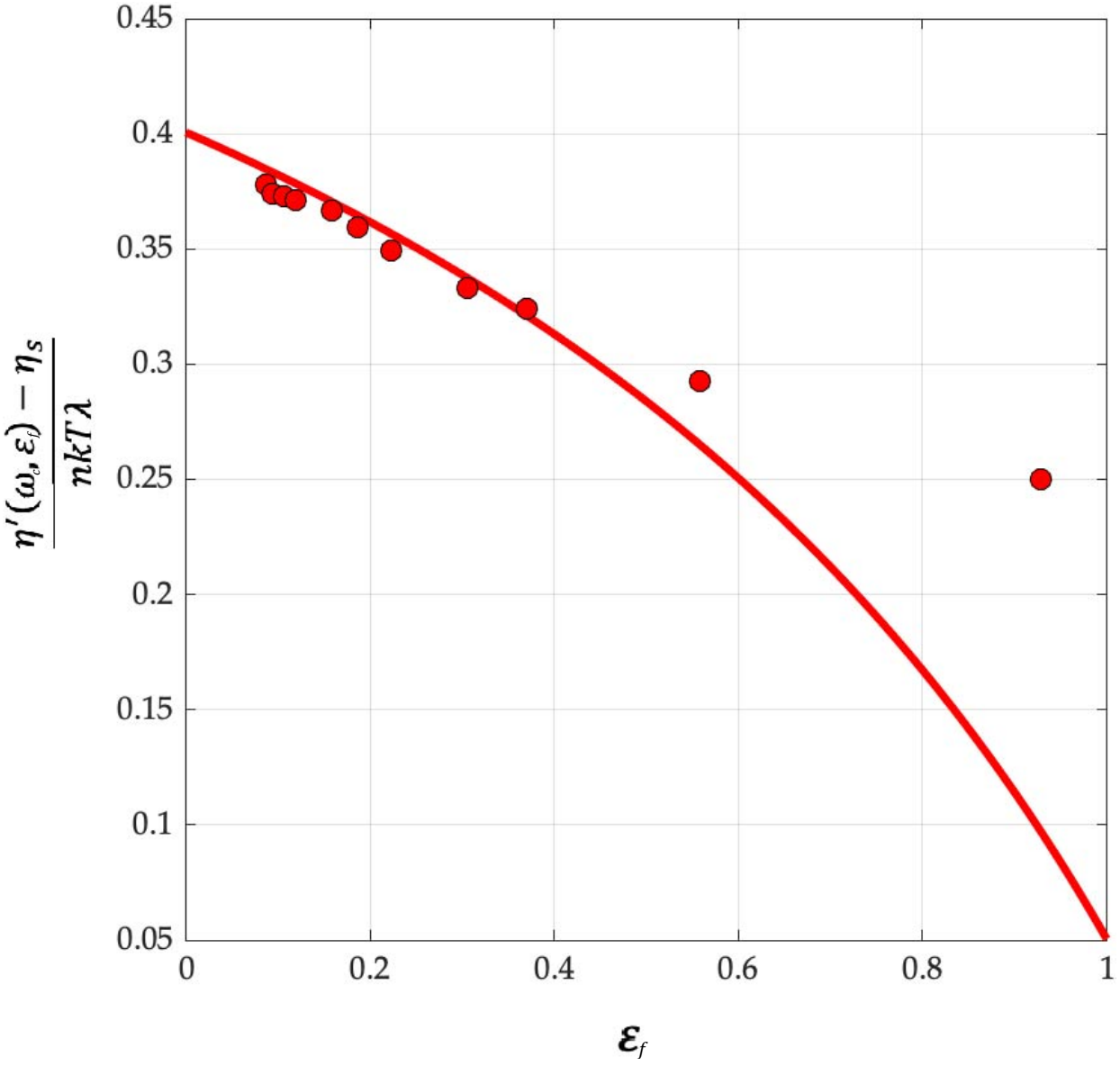

Figure 11: Eq. (22) fitted to $\eta'(\omega_c, \varepsilon_f)$ measurements of polystyrene in diethylphthalate at $c = 0.15$ mg/mL with $nkT = 1.852$ Pa, $T = 24$°C and $\omega_c = 31.6$ rad/s, with $\lambda = 1.00$ s and $L = 0.13$ mm. Entangled; $cM_w/c^* = 30 \times 10^9$ g/L.

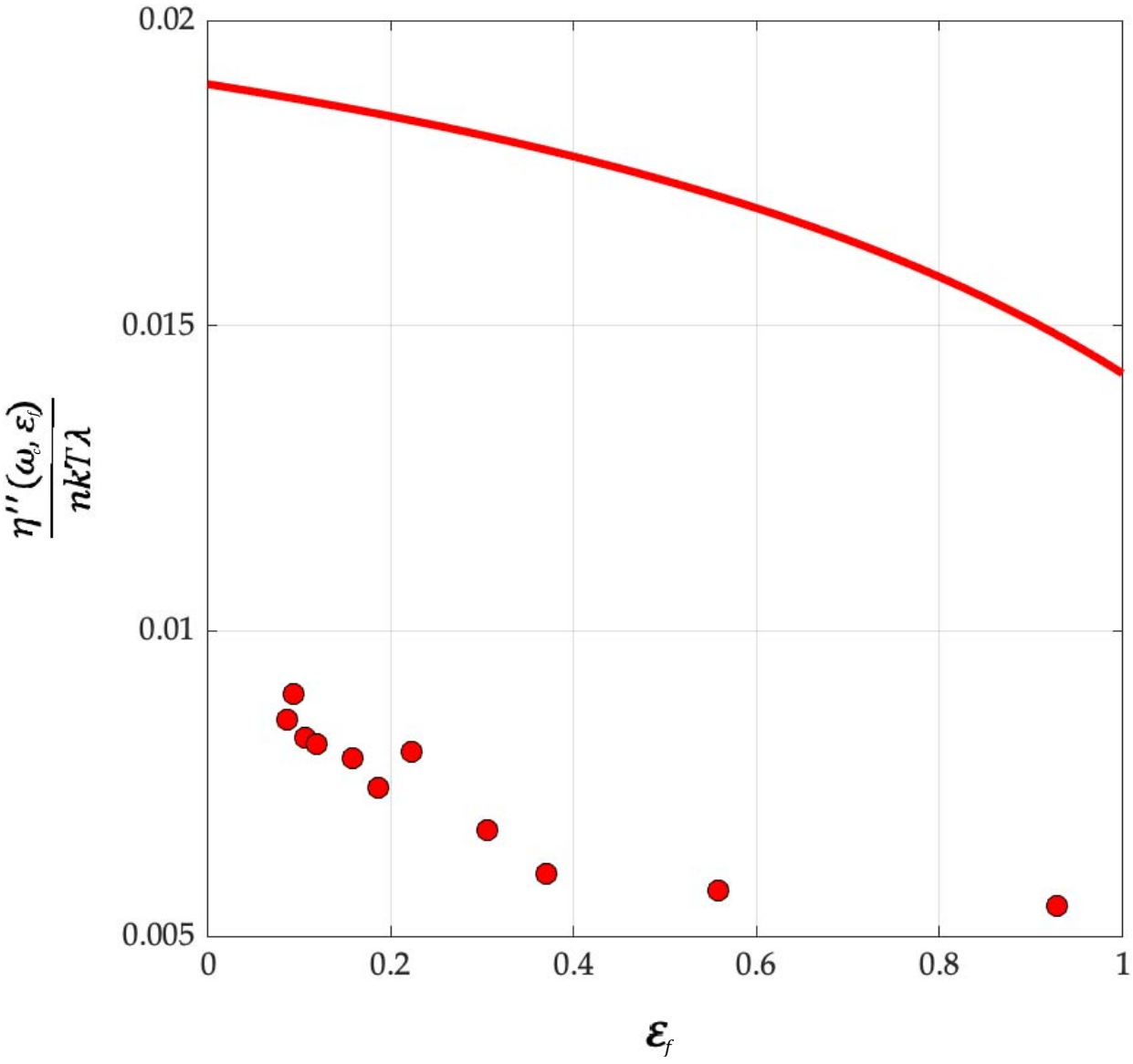

Figure 12: $\eta''(\omega_c, \varepsilon_f)$ from Eq. (23) evaluated using parameters from Eq. (22) fitted to $\eta'(\omega_c, \varepsilon_f)$ measurements of polystyrene in diethylphthalate at $c = 0.15$ mg/mL with $nkT = 1.852$ Pa, $T = 24$°C and $\omega_c = 31.6$ rad/s, with $\lambda = 1.00$ s and $L = 0.13$ mm. Entangled; $cM_w/c^* = 30 \times 10^9$ g/L.

Chapter 3: Macromolecular Microfluidic Concentrators

Reproduced from Coombs, S.J., K. Tontiwattanakul and A.J. Giacomin, "Macromolecular Microfluidic Concentrators," *Physics of Fluids*, **34**(10), 103115 (October, 2022), pp. 1-7. Feature article [4], with the permission of AIP Publishing.

Microfluidic design, fabrication and experiments have developed rapidly, leading to lab-on-chip separation or fractionation as in particle sorting [7] or cell sorting [8] or separation of soluble substances [61]. By *microfluidic*, we mean that the transverse dimension of the flow channel is microscopic. In this paper, we concern ourselves with flow phenomena arising when macromolecular dimensions and the transverse dimension of the flow channel are of the same order of magnitude, or nearly so.

In this work, we shall design a continuous concentrator for macromolecular solutions flowing through a microfluidic slot (Figure 13). By *concentrator*, we mean that one stream emerging from the microfluidic device will be more concentrated with polymer than the feed stream. Our concentrator design corresponds to the special case of Figure 1 of [61], with zero merging solvent flow on the left. We employ a velocity gradient to drive this fractionation by orientational diffusion. Our design relies on the analytical solutions for orientational diffusion under laminar pressure-driven slot flow through a microchannel [5]. The evolution of polymer concentration profiles in pressure-driven flows has been observed in the cross-slot (Fig. 1B of [36]), and by numerical simulation in the square duct [62]. Our work focusses on polymer migration in heterogeneous flow fields, and is not to be confused with particle migration about which much has been written (Figure 1 of [63]; [64]).

Using rigid dumbbell theory ([43]; Chapter 14 of [65]), we provide analytical solutions for the design of our microfluidic macromolecular hydrodynamic chromatograph. By *rigid*, we mean that the macromolecular orientation contributes

much more to the rheology of the polymeric liquid than any macromolecular deformation [66]. We arrive at our design through the use of well-known confinement-driven composition profiles (Eq. (3.22) of [5]). Using a pair of razor-sharp blades, our design separates the slot flow into a symmetric core inner slot (concentrated) between two outer slots (diluted). For the design of Figure 13, we seek analytically, the appropriate blade leading edge separation for sufficient fractionation, and for a given confinement and given shear rate.

Polymeric fluids, in contrast to Newtonian, exhibit complex flow behaviors such as polymer migration. As such, predicting this macromolecular behavior is essential for design, control, and optimization of polymer processes. One good way of explaining the elastic properties of liquids in the bulk is by considering their orientation distributions under flow [37,38,39,40]. Integrating these distributions in phase space yields the rheological properties (Section **IX.** of [6,41]). We can link the flow migration responses to macromolecular orientation [35]. When the macromolecule is replaced by identical spheres of fixed center-to-center separation, L, we call its replacement a rigid dumbbell, shown in Figure 13. We choose the rigid dumbbell suspension because it is the simplest relevant model macromolecule [43]. By *relevant*, we mean that, at least qualitatively, it captures the observed behaviours for the most measured viscoelastic material functions [43,42].

Experimentally, confined polymer solutions have deviated from homogeneity, such that the polymer solutions in a microchannel exhibit concentration heterogeneity [67,68]. A vertical concentration gradient of rigid dumbbells thus develops across the microchannel. For confined pressure-driven slot flow of a rigid dumbbell suspension, Stasiak and Cohen [5] arrive at:

$$v_{x,s} = v_0 \left[1 - \left(\frac{y}{B}\right)^2\right] \tag{42}$$

and the migration velocity difference of rigid dumbbells by:

$$v_{x,p} - v_{x,s} = -\frac{v_0}{12}\left(\frac{L}{B}\right)^2 \left[\left(1 - \frac{3}{70}\varepsilon^2 + \frac{20939}{462000}\varepsilon^4 + O(\varepsilon^6)\right) - \left(\varepsilon\frac{y}{B}\right)^2 \left(\frac{18}{35} - \frac{20939}{38500}\varepsilon^2 + O(\varepsilon^4)\right) + \left(\varepsilon\frac{y}{B}\right)^4 \left(\frac{1326}{1925} + O(\varepsilon^2)\right)\right] \tag{43}$$

wherein:

$$\varepsilon \equiv \lambda\dot{\gamma}^0 \frac{L}{B} \tag{44}$$

in which the Weissenberg number, $\lambda\dot{\gamma}^0$, reflects the amount of nonlinearity in the flow. For our pressure-driven slot flow, $\dot{\gamma}^0$ is the wall shear rate (see Subsection 5.7 of [69]; [70,71,72]). Companion Eqs. (42) and (43) give the velocity of the solvent and the relative velocity of the polymer respectively. In Eq. (44), the rigid dumbbell confinement is L/B [2], so that ε is the product of the Weissenberg number and the confinement.

Though our work here is mainly motivated by curiosity, the many applications for this work have not escaped our attention. We explore these applications in the Worked Example. For our symbols, dimensional and nondimensional, respectively listed in Table 1 and Table 2, we follow those of the corresponding textbook treatments, EXAMPLE 16.7-1 of [65] (or EXAMPLE 13.6-1 of [73]).

3.1. Method

To understand the motion of the rigid dumbbells, the dimensionless polymer concentration is modelled as:

$$x_p \equiv \frac{c_p}{c_s + c_p} = \frac{1}{1 + c_s/c_p} = \frac{1}{1 + x_s/x_p} \tag{45}$$

where c_p and c_s are the concentrations of the polymer and solvent respectively. We must then get an expression for x_s/x_p. We investigate the polymer concentration in a slice of the microchannel:

$$x_p \equiv \frac{q_p}{q_s + q_p} = \frac{q_p/A}{q_s/A + q_p/A} \tag{46}$$

where A is the area of the slice, and q_p and q_s are the volumetric flowrates of the polymer and solvent respectively. Further, we know that $q_i/A = v_{x,i}$, such that:

$$x_p \equiv \frac{v_{x,p}}{v_{x,s} + v_{x,p}} = \frac{1}{1 + v_{x,s}/v_{x,p}} \tag{47}$$

and for dilute solution, where:

$$v_{x,p} \ll v_{x,s} \tag{48}$$

and, therefore:

$$x_p \cong \frac{v_{x,p}}{v_{x,s}} \tag{49}$$

From Eq. (47), we learn that when $v_{x,s} = v_{x,p}$, $x_p = \frac{1}{2}$, we would have a homogeneous solution. We investigate the velocities of the polymer and solvent presently.

The dimensionless velocity profile given by the Poiseuille profile (from Fig. 1. of [14]):

$$\frac{v_{x,s}}{v_0} = 1 - \left(\frac{y}{B}\right)^2 \tag{50}$$

where v_0 is the maximum velocity at the mid-plane of the microchannel, B is half the microchannel height, and y/B is the dimensionless position along the vertical axis. The migration velocity difference, that is, the vertical difference of the rigid dumbbell along the microchannel is (Eq. (3.22) of [14]):

$$\frac{v_{x,p}-v_{x,s}}{v_0}=-\frac{1}{12}\left(\frac{L}{B}\right)^2\left[\left(1-\frac{3}{70}\varepsilon^2+\frac{20939}{462000}\varepsilon^4+O(\varepsilon^6)\right)\right.$$
$$\left.-\left(\varepsilon\frac{y}{B}\right)^2\left(\frac{18}{35}-\frac{20939}{38500}\varepsilon^2+O(\varepsilon^4)\right)+\left(\varepsilon\frac{y}{B}\right)^4\left(\frac{1326}{1925}+O(\varepsilon^2)\right)\right] \tag{51}$$

where, for zero confinement ($\varepsilon = 0$):

$$\frac{v_{x,p}-v_{x,s}}{v_0}=-\frac{1}{12}\left(\frac{L}{B}\right)^2 \tag{52}$$

Dividing Eq. (51) by Eq. (50) gives:

$$\frac{v_{x,p}-v_{x,s}}{v_{x,s}}$$
$$=\frac{-\frac{1}{12}\left(\frac{L}{B}\right)^2\left[\begin{array}{c}\left(1-\frac{3}{70}\varepsilon^2+\frac{20939}{462000}\varepsilon^4+O(\varepsilon^6)\right)\\-\left(\varepsilon\frac{y}{B}\right)^2\left(\frac{18}{35}-\frac{20939}{38500}\varepsilon^2+O(\varepsilon^4)\right)+\left(\varepsilon\frac{y}{B}\right)^4\left(\frac{1326}{1925}+O(\varepsilon^2)\right)\end{array}\right]}{1-\left(\frac{y}{B}\right)^2} \tag{53}$$

which simplifies as:

$$\frac{v_{x,p}}{v_{x,s}}$$
$$=1-\frac{\frac{1}{12}\left(\frac{L}{B}\right)^2\left[\begin{array}{c}\left(1-\frac{3}{70}\varepsilon^2+\frac{20939}{462000}\varepsilon^4+O(\varepsilon^6)\right)\\-\left(\varepsilon\frac{y}{B}\right)^2\left(\frac{18}{35}-\frac{20939}{38500}\varepsilon^2+O(\varepsilon^4)\right)+\left(\varepsilon\frac{y}{B}\right)^4\left(\frac{1326}{1925}+O(\varepsilon^2)\right)\end{array}\right]}{1-\left(\frac{y}{B}\right)^2} \tag{54}$$

For zero confinement of Eq. (54):

$$\frac{v_{x,p}}{v_{x,s}}=1-\frac{\frac{1}{12}\left(\frac{L}{B}\right)^2}{1-\left(\frac{y}{B}\right)^2} \tag{55}$$

which, on the mid-plane, gives:

$$\frac{v_{x,p}}{v_{x,s}} = \frac{v_{x,p}}{v_0} = 1 - \frac{1}{12}\left(\frac{L}{B}\right)^2 \tag{56}$$

and, at the wall:

$$\frac{v_{x,p}}{v_{x,s}} = -\infty \tag{57}$$

Since, $v_{x,p}/v_{x,s} > 0$, from Eq. (55), we glean:

$$\left(\frac{y}{B}\right)^2 < 1 - \frac{1}{12}\left(\frac{L}{B}\right)^2 \tag{58}$$

to which Eq. (54) is subject. Further, this inequality tells us that Eq. (54) is not valid close to the wall when y approaches B.

We next seek to nondimensionalize our main result, Eq. (47) [with Eq. (54)]. For this we choose the mid-plane concentration ($y/B = 0$):

$$x_c = \frac{1}{1 + \dfrac{12}{12 - \left(\frac{L}{B}\right)^2\left(1 - \frac{3}{70}\varepsilon^2 + \frac{20939}{462000}\varepsilon^4\right)}} \tag{59}$$

so that:

$$\frac{x_p}{x_c} = \left[1 + \frac{12}{12 - \left(\frac{L}{B}\right)^2\left(1 - \frac{3}{70}\varepsilon^2 + \frac{20939}{462000}\varepsilon^4\right)}\right]\frac{1}{1 + v_{x,s}/v_{x,p}} \tag{60}$$

which we will use presently.

3.2. Results

Substituting Eq. (54) into Eq. (60) yields our normalized confinement concentration profile:

$$\chi_p \equiv \frac{x_p}{x_c} = \frac{1+\dfrac{12}{12-\left(\frac{L}{B}\right)^2\left(1-\frac{3}{70}\varepsilon^2+\frac{20939}{462000}\varepsilon^4\right)}}{1+\left\{1-\dfrac{\frac{1}{12}\left(\frac{L}{B}\right)^2\left[1+f\left(\varepsilon,\frac{y}{B}\right)\right]}{1-\left(\frac{y}{B}\right)^2}\right\}^{-1}} \tag{61}$$

which defines χ_p, and is subject to Eq. (58), and where:

$$f\left(\varepsilon,\frac{y}{B}\right) \equiv \begin{array}{c}\left(-\frac{3}{70}\varepsilon^2+\frac{20939}{462000}\varepsilon^4+O(\varepsilon^6)\right)\\ -\left(\varepsilon\frac{y}{B}\right)^2\left(\frac{18}{35}-\frac{20939}{38500}\varepsilon^2+O(\varepsilon^4)\right)+\left(\varepsilon\frac{y}{B}\right)^4\left(\frac{1326}{1925}+O(\varepsilon^2)\right)\end{array} \tag{62}$$

Eq. (61) [with Eq. (62)] is the main result of this work. For dilute solution, we insert Eq. (49) into Eq. (60) to get:

$$\chi_p \cong \left[1+\frac{12}{12-\left(\frac{L}{B}\right)^2\left(1-\frac{3}{70}\varepsilon^2+\frac{20939}{462000}\varepsilon^4\right)}\right]\left\{1-\frac{\frac{1}{12}\left(\frac{L}{B}\right)^2\left[1+f\left(\varepsilon,\frac{y}{B}\right)\right]}{1-\left(\frac{y}{B}\right)^2}\right\} \tag{63}$$

which is our main result, and which we illustrate in Figure 14, Figure 15, and Figure 16 (parametrized with arbitrary values of confinement). These figures give concentration profiles for each of three different Weissenberg numbers. From these figures we glean Table 5, namely the confinements L/B values for the three Weissenberg numbers.

Setting Eq. (63) to zero gives ($\chi_p = 0$):

$$\frac{L}{B} = \sqrt{\frac{12\left[1-\left(\frac{y_i}{B}\right)^2\right]}{1+f\left(\varepsilon,\frac{y_i}{B}\right)}} \tag{64}$$

where y_i/B are the x-intercepts from Figure 14, Figure 15, and Figure 16. We thus illustrate Eq. (64) [with Eqs. (44) and (62)] in Figure 17 by plotting these x-intercepts. Eq.

(64) [with Eqs. (44) and (62)] is quartic in both L/B and y_i/B. We leave its exact solution for another day.

3.2.1. Worked Example: Atactic Polystyrene

Given a suspension of dumbbells of length, $L = 3.38 \times 10^{-5}$ m, pumped through a slot of a gap of $2B = 0.4$ mm, at temperature, $T = 25$°C, with wall shear rate, $\dot{\gamma}^0 = 71\ 1/\text{s}$, find the minimum blade leading edge separation for complete fractionation. The dumbbells are of bead diameter, $d = 1.50 \times 10^{-5}$ m, and suspended in a solvent of $\eta_s = 2.28 \times 10^{-7}$ Pa s.

We begin by calculating the relaxation time for rigid dumbbells (using Eq. (6) of [6]):

$$\lambda_0 = \frac{\pi d \eta_s L^2}{4kT} = 0.746\ s \tag{65}$$

Next, we determine the Weissenberg number [Eq. (44)]:

$$\text{Wi} = \lambda_0 \dot{\gamma}^0 = 53 \tag{66}$$

From the given dumbbell length, L, and slot gap, B, we get:

$$\frac{L}{B} = 0.169 \tag{67}$$

and with known Weissenberg number from Eq. (66), the concentration curve [Eq. (63)] is determined, illustrated in Figure 18. From Figure 18, we see that $y_i/B = 0.180$. Thus, for complete fractionation, the blade leading edge separation must exceed $y_i/B = 0.180$.

Table 5: Confinement L/B results for varying Weissenberg number from Figure 14, Figure 15, and Figure 16.

	$\mathbf{Wi = 0.5}$	$\mathbf{Wi = 1}$	$\mathbf{Wi = 10}$
$\boldsymbol{y_i/B}$	$\boldsymbol{L/B}$		
0	3.1851	2.3568	0.5465
0.2	3.0600	2.2100	0.5100
0.4	2.7700	1.9500	0.4350
0.6	2.4000	1.6400	0.3700
0.8	1.9000	1.3200	0.2950
1	0.5000	0.6000	0.1800

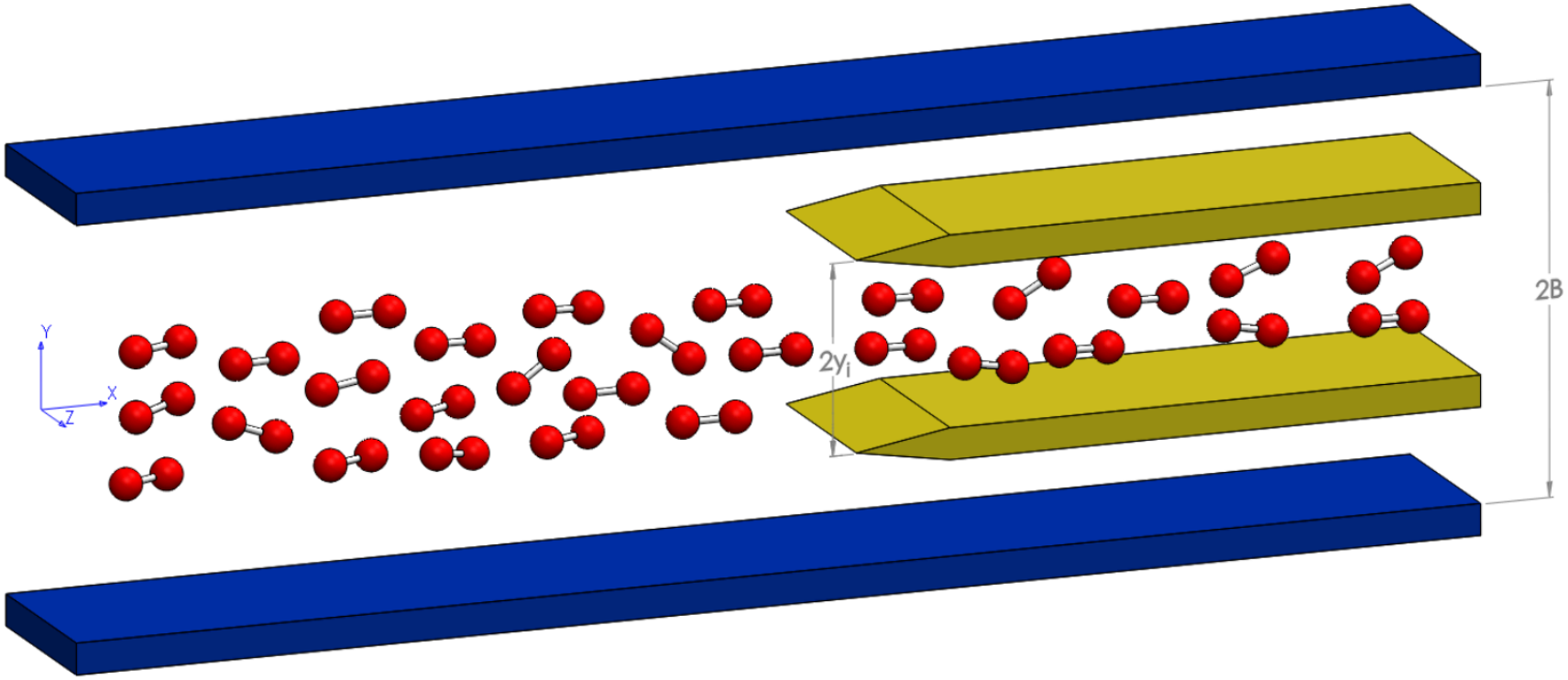

Figure 13: Continuous concentrator for macromolecular solutions flowing through a microfluidic slot.

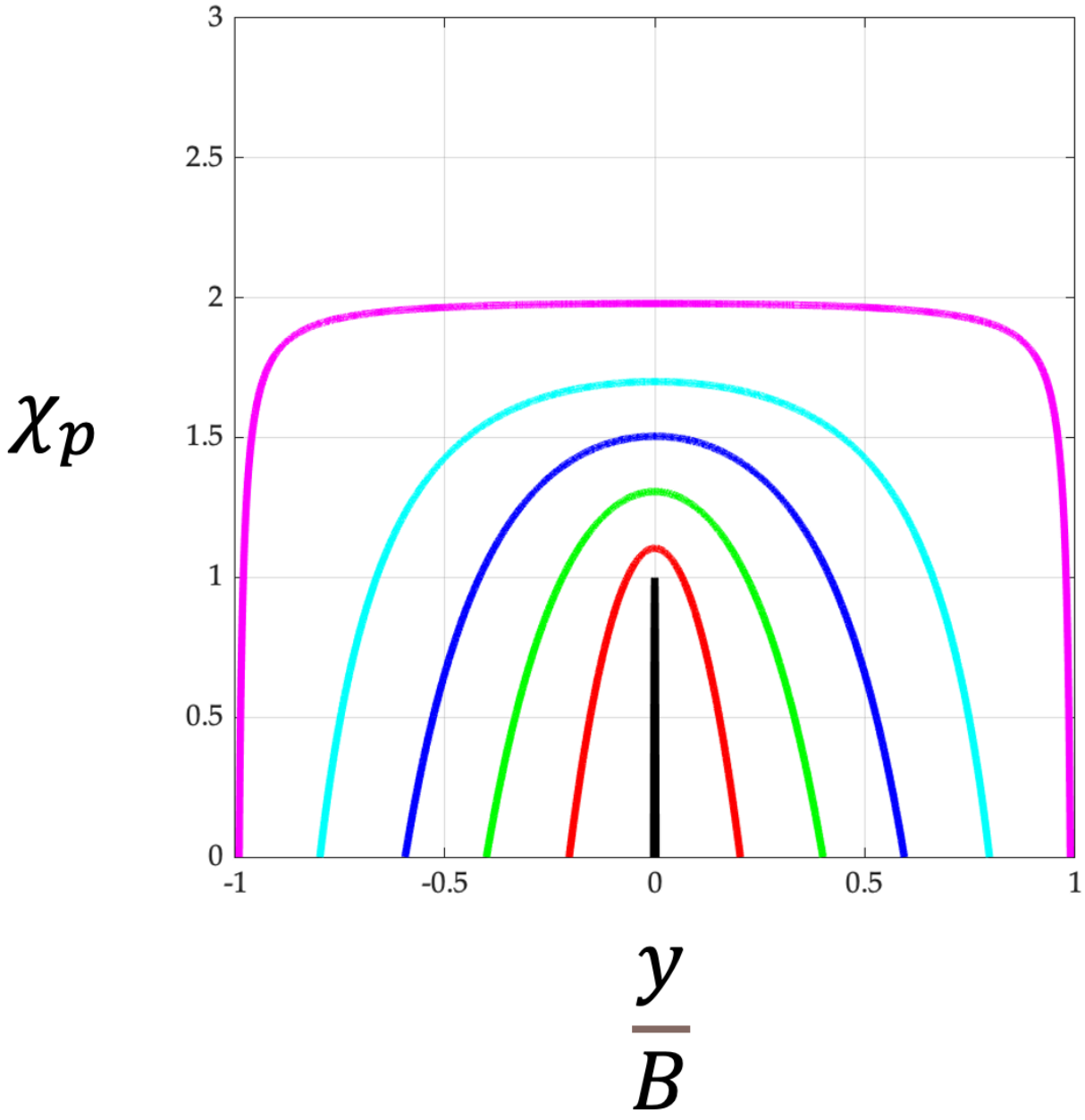

Figure 14: $\chi_p(L/B\,, y/B)$ from Eq. (63) for varying L/B at Wi $=$ 0.5 [black: $L/B =$ 3.1851; red: $L/B = 3.0600$; green: $L/B = 2.7700$; blue: $L/B = 2.4000$; cyan: $L/B =$ 1.9000; magenta: $L/B = 0.5000$].

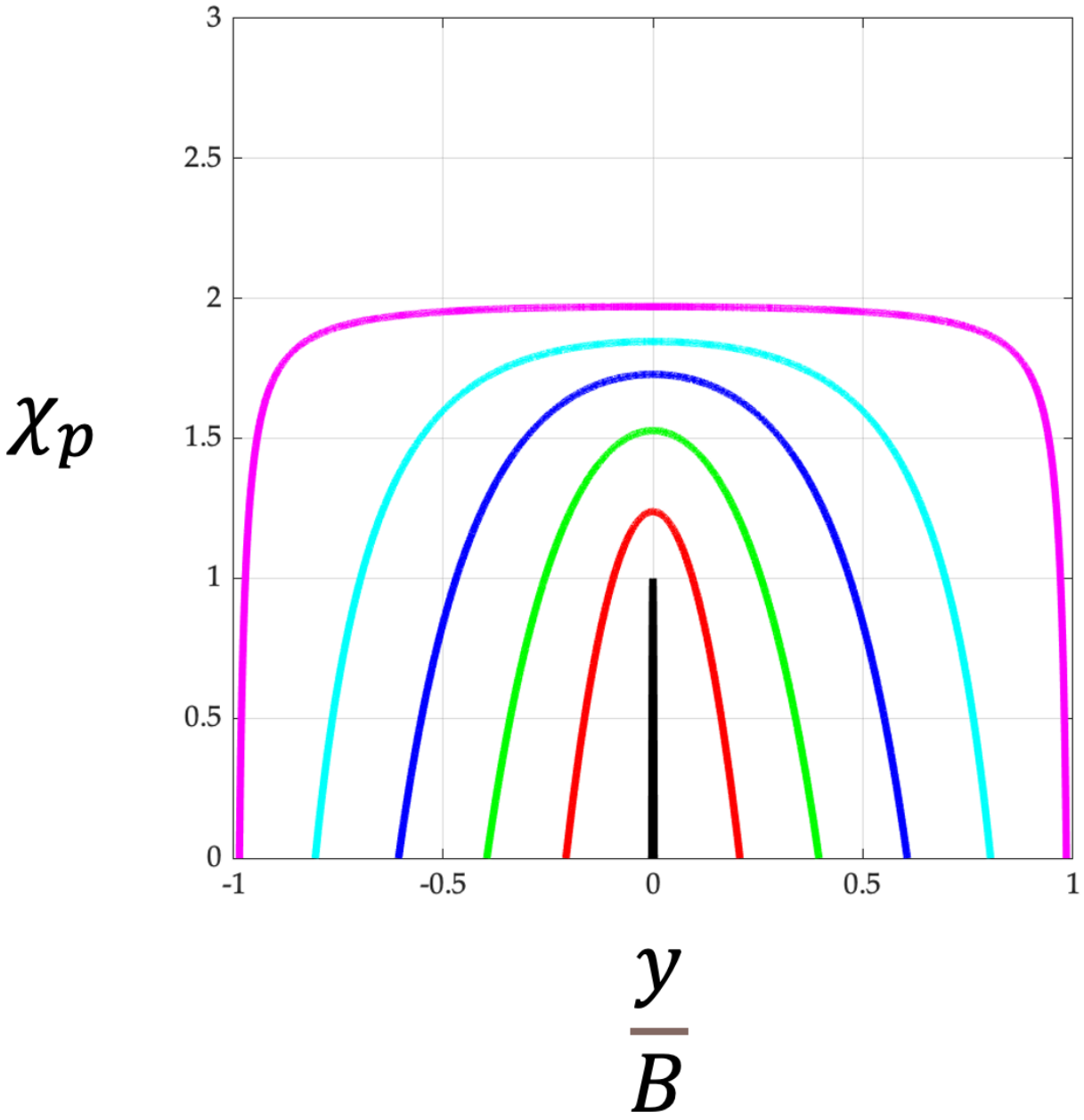

Figure 15: $\chi_p(L/B\,, y/B)$ from Eq. (63) for varying L/B at $Wi = 1$ [black: $L/B = 2.3568$; red: $L/B = 2.2100$; green: $L/B = 1.9500$; blue: $L/B = 1.6400$; cyan: $L/B = 1.3200$; magenta:$L/B = 0.6000$].

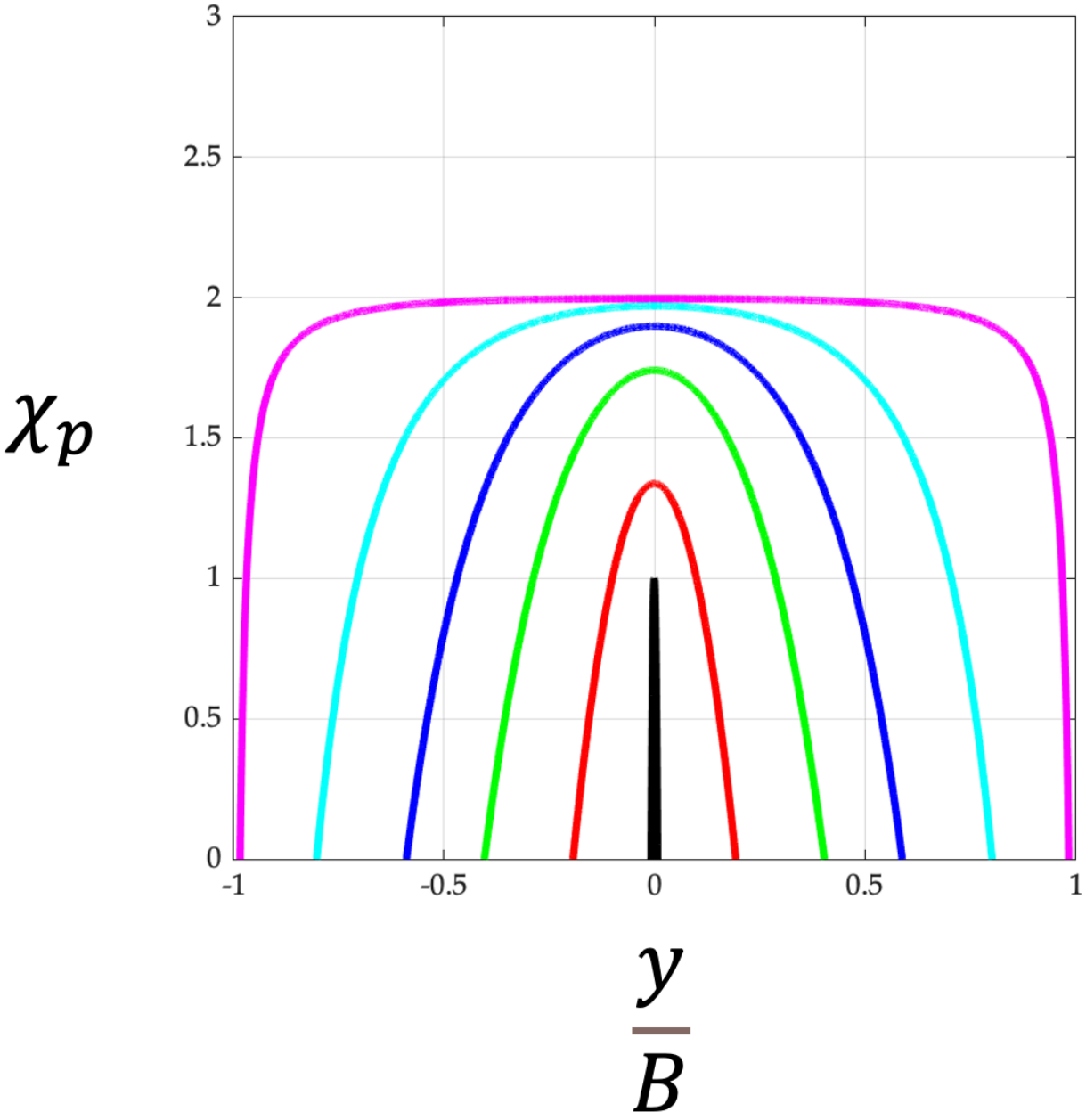

Figure 16: $\chi_p(L/B\,, y/B)$ from Eq. (63) for varying L/B at $Wi\ =\ 10$ [black: $L/B\ =$ 0.5465; red: $L/B\ =$ 0.5100; green: $L/B\ =$ 0.4350; blue: $L/B\ =$ 0.3700; cyan: $L/B\ =$ 0.2950; magenta: $L/B\ =$ 0.1800].

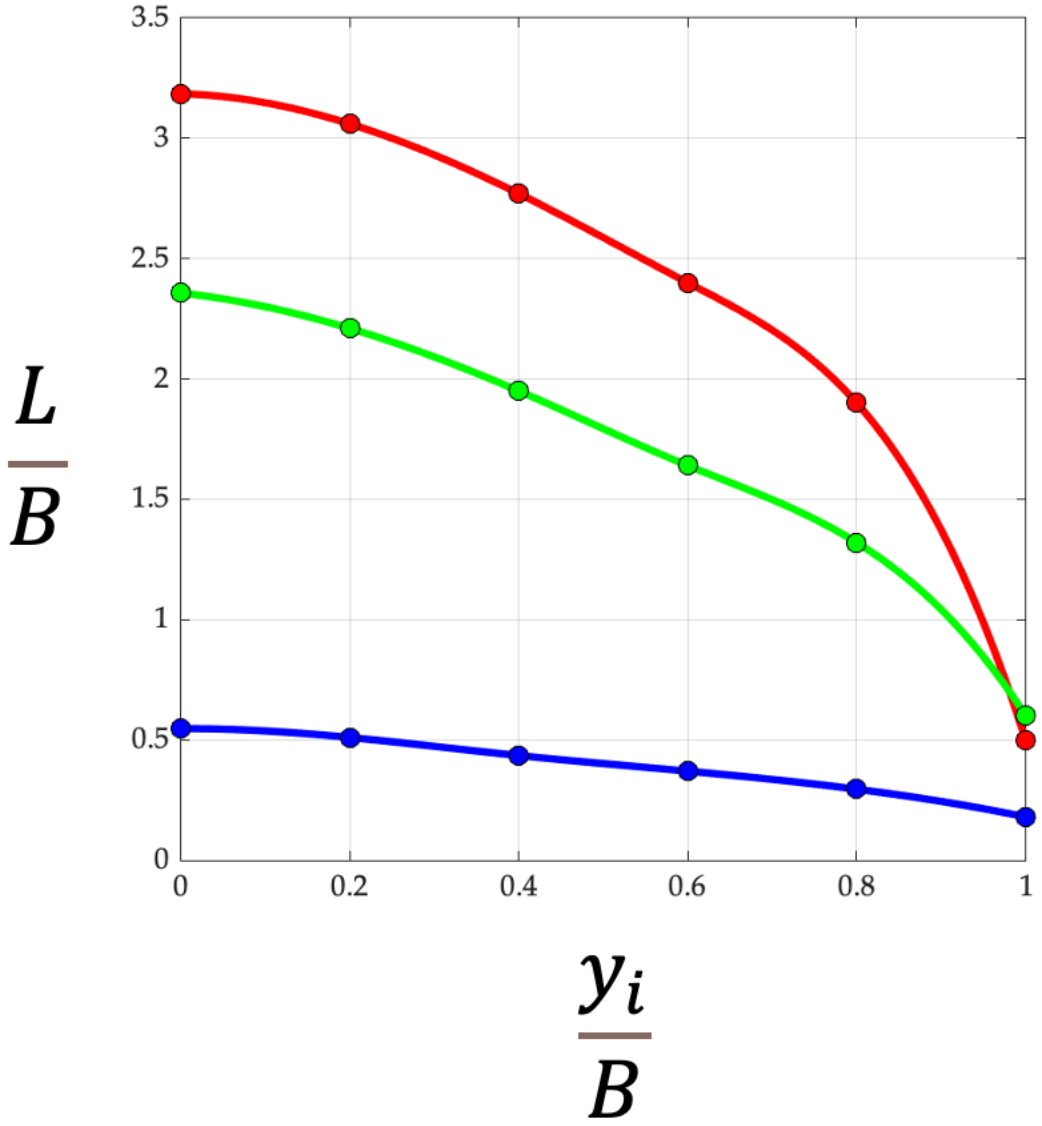

Figure 17: L/B *versus* y_i/B for varying Weissenberg number [red: Wi $=$ 0.5; green: Wi $=$ 1 ; blue: Wi $=$ 10] with y_i/B points from x-intercepts of Figure 14, Figure 15, and Figure 16.

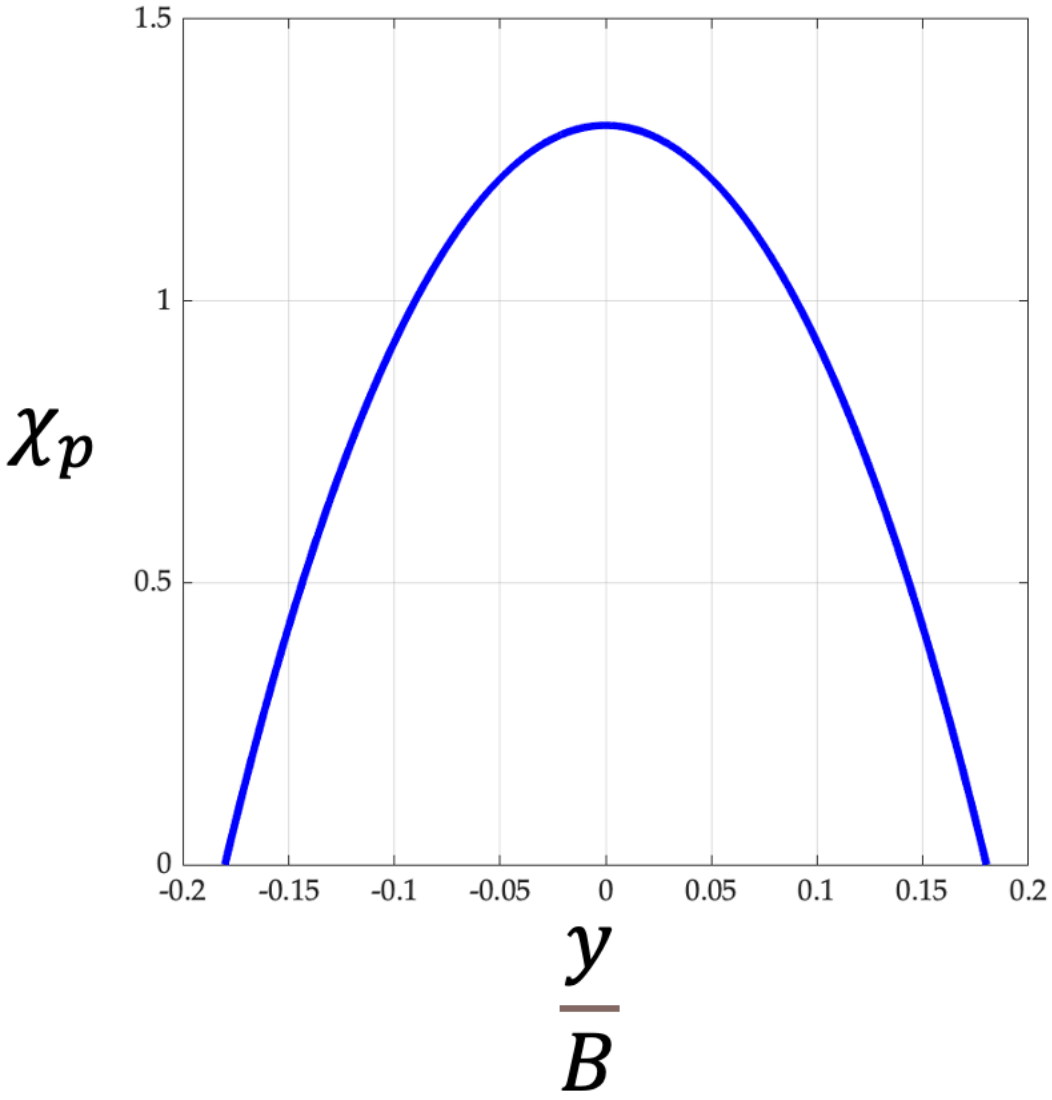

Figure 18: $\chi_p(L/B\,, y/B)$ from Eq. (63) for $y_i/B = 0.180$ and $Wi = 53$.

Chapter 4: Fabrication of Microfluidic Concentrators

Microfluidic devices perform reactions, separations, and detection in many applications, and behave as microreactors [74,75,76], micromixers [77,78,79,80], lab-on-chip [81,82,83], organ-on-a-chip [84,85,86] and sorters and separators [7,9]. Though much is understood on passive and active particle [7,87,88,89,90,91,92] and cell separation [8,93,94,95,96,97], polymer solutions in microfluidics have yet to be thoroughly studied except in the form of numerical and simulation studies [63,34,33,98]. By *passive*, we mean channel geometry and inertia control the flow and migration of the fluid inside the microchannels [10]. By *active*, we mean that the fluid within the microfluidic channels are manipulated using an external force, such as acoustic pressure fields, electric fields, magnetic fields, optical or electromagnetic fields and thermal gradients [10]. Inertial and orientation focusing passive separation occurs under laminar flow conditions, in which non-Newtonian viscoelastic fluids migrate laterally within the microchannel. This migration has been investigated extensively for particle sorting but are limited in the case of polymer solutions. Nguyen *et al.* investigates continuous separation of heterogeneous polystyrene and solvent injected into the microfluidic device and relies on diffusion characteristics [61]. These works however, are silent on homogeneous polymer solutions [67,68].

Particle separation is not to be confused with polymer solution separation in rigid dumbbell theory. According to general rigid bead-rod theory, orientation is the cause for non-Newtonian behaviour [42,43,35]. Within rigid dumbbell theory, a special case within general rigid bead-rod theory, polymers are replaced by rigid dumbbells (Chapter 14 of [45], [66]). Rigid dumbbells, in contrast to spherical particles, have orientation and the migration can therefore be predicted by the works of Stasiak and Cohen [5].

Common substrates used in the fabrication of microfluidic devices includes glass, silicon, metals, polymers, and ceramics [99], which are selected based on the desired design, material properties, manufacturability, and cost [100]. Microfluidic devices can be fabricated through direct manufacturing or a replication approach [100]. Direct manufacturing occurs through mechanical, energy assisted and MEMS-based methods whereas replication manufacturing methods include casting, hot embossing, and micro-injection moulding [100]. In the case of prototyping or low-volume production, soft lithography is used for silicone-based elastomers to mould or create a stamp in which Polydimethylsiloxane (PDMS), an elastomer, is frequently used ([100,101]; **Table 1** of [102]). Specifically, the method of replica molding is used by 3D-printing to form positive master mold in which PDMS is poured to create a channel mould (see **Figure 1.A** of [101]).

The polymer solution concentration at the outlets of these microfluidic devices can be measured or observed to determine the effectiveness of separation. Spectroscopy is a popular technique in the determination of chemical structure and analysis using the methods of UV, visible, IR, Raman, H NMR, C NMR, ESR and mass spectroscopy. Ultraviolet and Visible (UV-Vis) spectroscopy records the absorption regions of the electromagnetic spectrum of 200 – 800 nm [103]. A UV-Vis spectrophotometer records a UV-Vis spectrum by outputting a plot of wavelength versus absorbance (optical density). From the Lambert-Beer Law (Eq. (2.1) of [103]):

$$A_{LB} = m_a c l_s \tag{68}$$

in which the maximum absorption is used [104].

In this work, we present a microfluidic device that provides continuous, passive separation that relies on diffusion. The chip was designed as slot-flow and square duct

devices, such that the outlet concentrations can be compared with the predicted rigid dumbbell theory values (Eq. (63) of Section 3.2).

4.1. Materials and Methods

4.1.1. Microfluidic Device Design and Fabrication

Using microscope slides of 50 mm x 75 mm for the microfluidic separator platform, two microfluidic devices (slot flow, square duct) were fabricated. For the slot flow device, a 1,500 μm deep, 300 μm wide straight channel with one inlet and three outlets was used to verify to migratory response of the separation system (Figure 19). For the square duct device, a 300 μm deep, 300 μm wide straight channel with three outlets was used to verify to migratory response of the separation system (Figure 20). Following the fabrication outlined in [105], the channel was designed using SolidWorks and fabricated using soft lithography. Using an SLA 3D printer (ANYCUBIC Photon S, China) with 405 nm UV-sensitive resin with 50 μm layer thickness, moulds for the two microfluidic devices were fabricated. To prevent Polydimethylsiloxane (PDMS) from adhering to the mould [106], silanization was conducted by forming a monolayer of 1H,1H,2H,2H-perfluorooctyltriethoxysilane (MilliporeSigma, Burlington, MA, USA) on the surface of the mould using vapour deposition. PDMS (SYLGARD 184, Dow Silicones Corporation, Midland, MI, USA) was mixed in a 10:1 w/w ratio of base and curing agent [107]. After degassing for 30 minutes, the PDMS was poured into the moulds and cured at 70^{o}C for 30 minutes then left to sit at room temperature overnight. The cured PDMS was demoulded using a scalpel, then a biopsy puncher was used to create inlet and outlet holes. Using a plasma cleaner (Harrick Plasma, Ithaca, NY, USA) for plasma oxidation, the channel side of the PDMS surface and glass microscope slides were oxidized then immediately placed in contact to form a silicon-oxygen bond [108].

Using the concentrations and relaxation times outlined in Section 2.2.2., a relaxation time of $\lambda = 1.0\ s$ is selected for chip design. From **TABLE V** of [44] for a rigid dumbbell:

$$\frac{\lambda}{\lambda_0} = 1 \tag{69}$$

and approximating that residence time is equal to or greater than relaxation (orientation) time [114], flowrate of 1 $\mu L/min$, cross-sectional area of 90,000 μm^2:

$$t_r = \frac{z}{v_0} \tag{70}$$

a channel distance is calculated to be $z = 0.20\ cm$. To account for error, a channel distance of $z = 0.80\ cm$ was input into the SolidWorks design.

4.1.2. Materials

In this study, a 0.050 mg/mL polystyrene (Sigma-Aldrich, Lot#MKCB9723) solution was prepared in Ethylene Glycol. Polystyrene pellets of molecular weight 350,000 g/mol and polydispersity of 2.05 were dissolved and assumed to be homogeneous within the solution. The solvent, Ethylene Glycol, was selected due to polystyrene solubility and compatibility with PDMS [109].

4.1.3. Viscosity Measurements

The complex viscosity of the polymer solution will be measured using an Anton Parr rheometer for a frequency sweep of 0 to 50 rad/s at a shear strain amplitude of 0.30. Both the real and imaginary parts of the complex viscosity will be measured using parallel plate geometry at varying gaps. The viscosity will first be measured at the bulk ($\varepsilon = 0$) to determine the relaxation time of the solution. Using Eq. (21), the center-to-center length between macromolecules (L) can be determined. The parallel plates can then be set to gaps corresponding to the design of the microfluidic chips to investigate

the viscosity at specific confinements. This data will be fit to Eqs. (22) and (23) for $\eta'(\omega, \varepsilon)$.

4.1.4. Concentration Measurements

The concentration of the polymer solution at the outlet of the microfluidic chips will be measured using UV-Vis spectrophotometry for an absorbance versus wavelength of range 190-1,100 nm. Polystyrene exhibits UV spectra at around 290 nm [110] but will be confirmed using the 0.050 mg/mL solution. The concentration of the three channel outlets will be determined using The Lambert-Beer Law [104], which will be compared to Eq. (63).

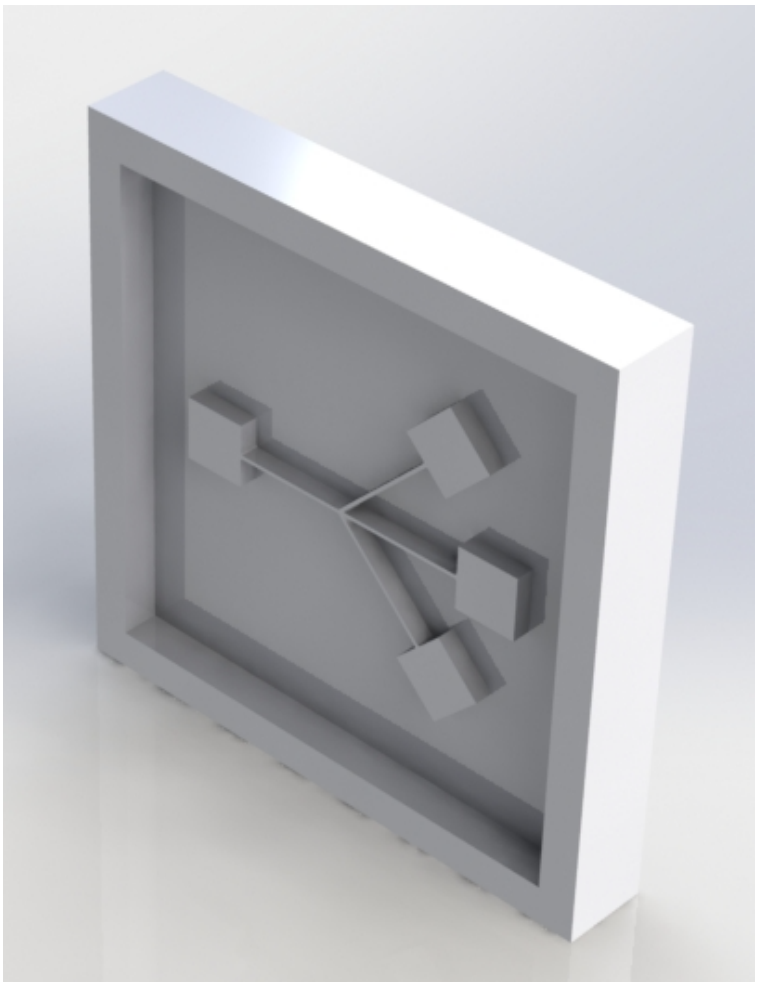

Figure 19: Design of slot flow microfluidic chip (SolidWorks rendering).

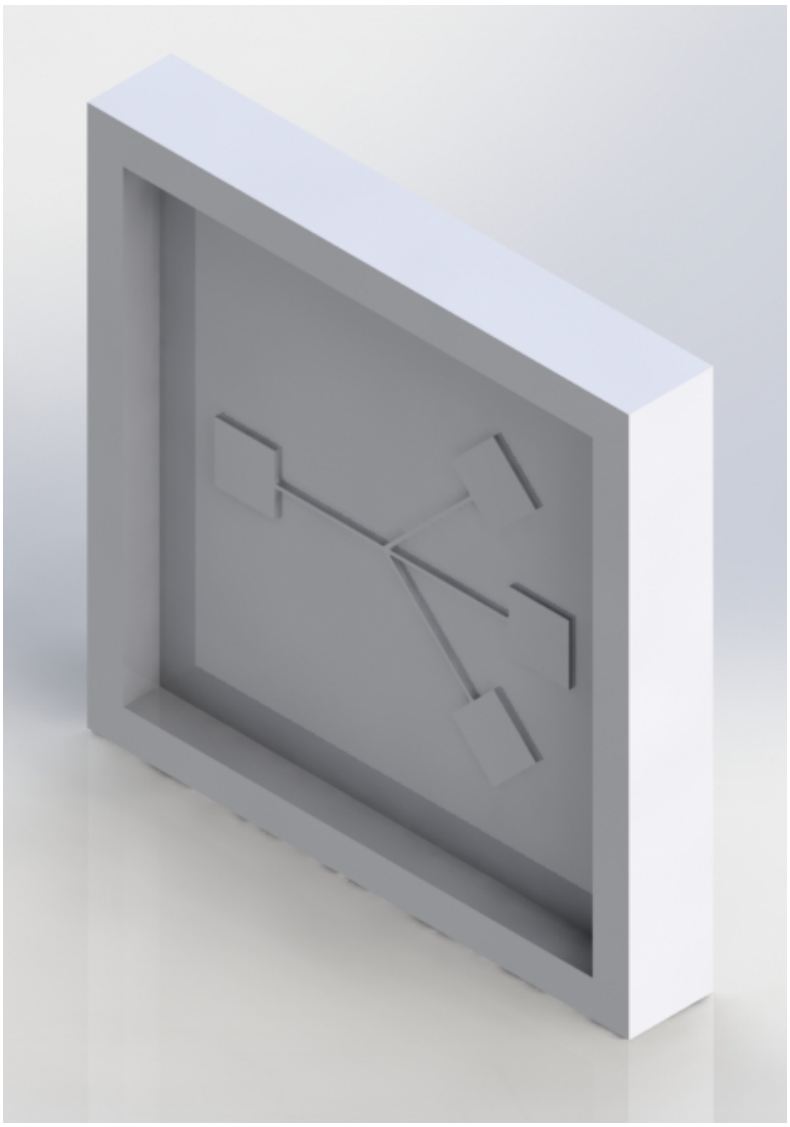

Figure 20: Design of square duct microfluidic chip (SolidWorks rendering).

Chapter 5: Conclusion and Recommendations

In Chapter 2, we find few complex viscosity confinement measurements in the literature. All but one of those we do find are for high confinement, where the $\eta'(\omega, \varepsilon_f)$ is increasing with ε_f (Fig. 9 of [56]). We know of no complex viscosity confinement data at all for polymer solutions. The literature will thus benefit from our new such confinement data for polystyrene in solution at low confinement (Figure 9, Figure 10, and Figure 11).

We have focused on the complex viscosity for which we began with the well-known confinement relations of [2], that is, Eqs. (22) and (23). Our literature review revealed just one set of complex viscosity confinement measurements performed at low enough confinement to see $\eta'(\omega, \varepsilon_f)$ decrease with ε_f (Fig. 11 of [57]). We find that the rigid dumbbell theory evaluated for complex viscosity at low confinement [Eqs. (22) or (30)] is accurate for the real part of the complex viscosity for the aqueous Carbopol suspension, and for all three of our organic polystyrene solutions. The decrease in viscosity upon decrease of the gap has also been interpreted in terms of slip at the wall. Our approach proceeds more simply, without slip. Specifically, in every instance, we find η' departing from zero confinement with a slope of $-1/4$, as the rigid dumbbell confinement theory predicts. We also find that the rigid dumbbell theory at low confinement [Eqs. (23) or (31)] to be qualitatively correct for *minus* the imaginary part. From the polystyrene solutions we learn that the fitted persistence length of the orientation, L_p, does not depend on concentration. We find for both agglomerated aqueous Carbopol suspensions or organic polystyrene solutions, L_p fitted to the confinement experiments to be about 0.1 mm, namely, two orders of magnitude larger than the macromolecular structures under study.

Whereas confinement relations are well-known for the complex viscosity in confinement [2], to our knowledge, no such confinement relations exist for the normal stress differences in small-amplitude oscillatory shear flow. Such relations have been derived for suspensions of rigid dumbbells in the bulk (Eqs. (13) and (21) of [111]). We leave the exploration of confinement and normal stress differences in small-amplitude oscillatory shear flow for another day.

We also expect future work on the steady-shear viscosity in low confinement. For this, for the rigid dumbbell suspension, we begin with the well-known result (Eq. (25a) of [2]):

$$\frac{\eta(\lambda\dot{\gamma})-\eta_s}{(\eta_0-\eta_s)|_{\varepsilon_f=0}} = \frac{1+\frac{1}{1-3\varepsilon_f/4}\sum_{k=1}^{\infty}\left\{\frac{1}{2}\varepsilon_f\bar{a}_k(1)+\varepsilon_f\bar{b}_k(1)+\left(1-\varepsilon_f\right)\frac{2}{5}E(k,1,2)(6)^{2k}(\lambda\dot{\gamma})^{2k}\right\}}{1+\frac{\varepsilon_f/2}{1-\varepsilon_f/2}\sum_{k=1}^{\infty}\bar{a}_k(1)(6\lambda\dot{\gamma})^{2k}} \tag{71}$$

where $\frac{2}{5}E(k,1,2)(6)^{2k}$ corresponds to the exact coefficients b_k in Table III of [112] so that:

$$\frac{\eta(\lambda\dot{\gamma})-\eta_s}{(\eta_0-\eta_s)|_{\varepsilon_f=0}} = \frac{1+\frac{1}{1-3\varepsilon_f/4}\sum_{k=1}^{\infty}\left\{\frac{1}{2}\varepsilon_f\bar{a}_k(1)+\varepsilon_f\bar{b}_k(1)+\left(1-\varepsilon_f\right)b_k(\lambda\dot{\gamma})^{2k}\right\}}{1+\frac{\varepsilon_f/2}{1-\varepsilon_f/2}\sum_{k=1}^{\infty}\bar{a}_k(1)(6)^{2k}(\lambda\dot{\gamma})^{2k}} \tag{72}$$

which in the limit as $\lambda\dot{\gamma}\to 0$, recovers Eq. (26), as it must. For $\bar{a}_k(1)$ and $\bar{b}_k(1)$ of Eq. (72), recursive relations are given respectively by Eqs. (19e) and (27a) of [2]. We leave the evaluations of these coefficients for another day.

Future work shall also refocus on the normal stress difference coefficients in steady-shear flow at low confinement. For the first normal stress coefficient, we begin with the well-known result, Eq. (26) of [2] with recursive relations Eqs. (27a) and (27b) of [2]. For

the second normal stress coefficient in steady-shear flow at low confinement, nothing is known. We leave these explorations for a later date.

Whereas Section **1**. of [1] derives the orientation distribution function for a suspension of rigid dumbbells between the walls of a confining simple shear flow fixture in small-amplitude oscillatory shear flow, we know of no experimental measurement of the orientation distribution gradient caused by the confinement. We leave this daunting task for another day.

In Chapter 3, we design a continuous concentrator for macromolecular solutions flowing through a microfluidic slot (Figure 13). Our design relies on the analytical solutions for orientational diffusion under laminar pressure-driven slot flow through a microchannel [5]. Using rigid dumbbell theory, we arrive at analytical solutions for the design of our microfluidic macromolecular hydrodynamic chromatography (Eq. (63) [with Eqs. (44) and (62)]). We arrive at our design through the use of well-known confinement-driven composition profiles [companion Eqs. (42) and (43)]. Using a pair of razor-sharp blades, our design separates the slot flow into a symmetric core inner slot (concentrated) between two outer slots (diluted) (see Figure 13). We discover a minimum dimensionless blade leading edge separation for complete fractionation [Eq. (64)], and that this decreases with confinement, L/B, and also decreases with dimensionless shear rate, $\lambda_0\dot{\gamma}^0$. In our analytical work, we discover that every occurrence of $\lambda_0\dot{\gamma}^0$ is multiplied by the confinement, but not every occurrence of confinement is multiplied by $\lambda_0\dot{\gamma}^0$.

To our knowledge, Stasiak and Cohen [5] are the only ones ever to derive an analytical solution for the concentration heterogeneity of a suspension of rigid dumbbells provoked by a heterogeneous flow field. They did so for pressure-driven

microfluidic slot flow (Eq. (3.22) of [5]). No one has arrived at such an analytical solution for any other pressure-driven microfluidic geometry. The most commonly used pressure-driven microfluidic geometry is the square duct (FIGS. 1 and 2 of [**62**]). We leave the daunting task of polymer migration in the square duct for another day. Further, our main results (Eq. (63) [with Eqs. (44) and (62)]) are for a rectangular slot, but for those interested in microfluidic annuli [113], if we neglect curvature, our main results can be rewritten approximately for microfluidic annuli.

Though this work confined itself to polymer solutions without dispersity, Eq. (43) could be rederived for a mixture of species from which the design of a fractionator for a disperse polymer solution could be launched. By *fractionator*, we mean that different fractions of the disperse polymer solution would result from different blade separations. To account for such dispersity, we would follow the well-known method of **PROBLEM 14C.2** of [65] (see also **§26.** of [43]). Of course, when the blade separation subceeds the y_i/B of Eq. (63), our microfluidic device will deliver partial fractionation. Whereas this work has focussed on exploiting fractionation in the microfluidic slot, our main results will be equally useful to those seeking to avoid, minimize or mitigate polymeric orientational fractionation.

We know our main results to be accurate only to within the three truncated orders of Eq. (62). We know our three truncated orders of Eq. (62) to be $O(\varepsilon^6)$, $O(\varepsilon^4)$, and $O(\varepsilon^2)$ respectively. The accuracy of our main results (Eq. (63) [with Eqs. (44) and (62)]) will therefore be affected thusly. We leave these higher order extensions of Eq. (62) for future work. For orientational migration of a polymer in a pressure-driven microfluidic channel, we know of no experimental data. The manufacture of a microfluidic device

with the required razor-sharp blades may be challenging. We leave this measurement for future work.

We have delimited this work to the simplest relevant model of a macromolecule, the rigid dumbbell. For the complex viscosity, Hassager has generalized this theory to general rigid bead-rod theory ([114]; EXAMPLE 16.7-1 of [65]; [44]). However, the Stasiak-Cohen [5] approach requires the steady shear viscosity. To extend Stasiak-Cohen [5] for rigid dumbbells for other structures, we would get the steady shear viscosity for general rigid bead-rod theory by continuing Eqs. (17) and (18) of Hassager [114], and then evaluating the result in the limit as $\lambda\omega$ goes to zero.

Eq. (3.22) of [5] is for steady state, in the limit of infinite time, and is thus silent on: (1) how long after startup it will take for the concentration profile of our main results (Eq. (63) [with Eqs. (44) and (62)]) to set up, (2) how long the slot must be before reaching the sharp edges of the fractionating blades, and (3) the corresponding effects of viscous dissipation and fluid inertia on minimum slot length.

Whereas the Stokes flow velocity field around each bead of the rigid dumbbell may interfere, Stasiak-Cohen [5] is silent on these hydrodynamic interactions. These interferences are normally accounted for using the Oseen tensor [115]. We leave the task of incorporating these hydrodynamic interactions into the heterogeneous pressure-driven slot flow for another day.

Whereas there are many types of microfluidics separators requiring an applied external field [3], ours does not. Controlling ours, for a fixed blade position, thus requires either controlling the wall shear rate, or the relaxation time (through the polymer solution temperature). For the latter, we get the wall shear rate by differentiating Eqs. (42) and (43), and evaluating the result at the wall.

From our main results (Eq. (63) [with Eqs. (44) and (62)]), we find a lower critical Weissenberg number for fractionation just below one-half (Figure 14) so that, without sufficient flow, we get no fractionation. We leave the intriguing determination of this pure number for another day. By contrast, the confinement itself of Eq. (63) is unbounded.

In Chapter 4, we design and fabricate a passive, continuous concentrator (exploiting the theory presented in Chapter 3) that relies on macromolecular migration for slot-flow (Figure 19) and square duct microchannels (Figure 20). Our solvent within the dilute polymer solution of 0.050 mg/mL polystyrene and ethylene glycol was selected based on polymer solubility and compatibility with the fabrication material of soft lithography (PDMS).

We know of no concentration measurements for microfluidic separators relying on polymer orientation. For these, we would choose a polymer solution of 0.050 mg/mL of polystyrene and ethylene glycol, and measure the real and imaginary parts of its complex viscosity in parallel disk geometry at varying gap. These measurements will be compared to our rigid dumbbell theory of Chapter 2 to get the solution transport properties. We would then measure the three outlet solution concentrations from our microfluidic device. These would be measured using UV-Vis spectrophotometry exploiting the Lambert-Beer law. We leave this important work for another day.

Our rigid dumbbell theory presented in Chapter 3 applies to slot-flow polymer migration within a microchannel. This thesis is silent on other microchannel geometries. As such, we fabricated our microfluidic devices to align with this theory for comparison. As we expand our knowledge through the evaluation of rigid dumbbell theory into other geometries, we will also fabricate and test these channel geometries to obtain experimental measurements. For instance, should microfabrication someday

allow it, we would fabricate a tubular microfluidic separator with a concentric cylindrical blade, or even a bank of these. We leave these daunting tasks for another day.

About the Author

Coombs is recognized as a *star peer-reviewer* by *Physics of Fluids* [116]. She also operates her own consulting practice, *Coombs & Associates*, where she provides expert witness support services in patent litigation, products liability, and consulting in rheology. Coombs has published extensively on rheology [11,12,13,14,3,4,117,118,119].

Coombs's is also active civically. Steacy served as elected President of the Chemical Engineering Graduate Student Association (CEGSA). She also serves as elected Vice-President Graduate of the Society of Graduate and Professional Students (SGPS). Coombs also runs a Chemistry and Chemical Engineering graduate student mentorship program called *Bonds For Success* in partnership with the Chemical Institute of Canada (CIC) Kingston Local section and CIC Toronto.

References

[1] Park, O.O. and G.G. Fuller, "Dynamics of Rigid and Flexible Polymer Chains in Confined Geometries Part II: Time-Dependent Shear Flow," *Journal of Non-Newtonian Fluid Mechanics*, **18**, (1985), pp. 111-122.

[2] Park, O.O. and G.G. Fuller, "Dynamics of Rigid and Flexible Polymer Chains in Confined Geometries Part I: Steady Simple Shear Flow," *Journal of Non-Newtonian Fluid Mechanics*, **15**, (1984), pp. 309-329.

[3] Coombs, S.J., R. Pasquino and A.J. Giacomin, "Confinement and Complex Viscosity," *Physics of Fluids*, **33**(4), 053104 (2021), pp. 1-7. Special Collection: Celebration of Robert Byron Bird (1924-2020). Editor's pick.

[4] Coombs, S.J., K. Tontiwattanakul and A.J. Giacomin, "Macromolecular Microfluidic Concentrators," *Physics of Fluids*, **34**(10), 103115 (October, 2022), pp. 1-7. Feature article.

[5] Stasiak, W. and C. Cohen, "Dilute Solutions of Macromolecules in a Rectilinear Poiseuille Flow," *Journal of Chemical Physics*, **78**(1) (1983), pp. 553-559.

[6] Bird, R.B., A.J. Giacomin, A.M. Schmalzer and C. Aumnate, "Dilute Rigid Dumbbell Suspensions in Large-Amplitude Oscillatory Shear Flow: Shear Stress Response," *The Journal of Chemical Physics*, **140**(7), 074904 (2014), pp. 1-16.

[7] Sajeesh, P. and A.K. Sen, "Particle Separation and Sorting in Microfluidic Devices: A Review," *Microfluid Nanofluid*, **17**, pp. 1-52 (2013).

[8] Bhagat, A.A.S., H. Bow, H.W. Hou, S.J. Tan, J. Han and C.T. Lim, "Microfluidics for Cell Separation," *Med. Biol. Eng. Comput*. **48**, pp. 999-1014 (2010).

[9] Antfold, M. and T. Laurell, "Continuous Flow Microfluidic Separation and Processing of Rare Cells and Bioparticles Found in Blood – A Review," *Analytica Chimica Acta*, **965**, pp. 9-35 (2017).

[10] Gharib, G., I. Bütün, Z. Muganli, G. Kozalak, I. Namli, S.S. Sarraf, V.E. Ahmadi, E. Toyran, A.J. van Wijnen and A. Kosar, "Biomedical Applications of Microfluidic Devices: A Review," *Biosensors*, **12**(11) 1012 (2022).

[11] Coombs, S.J., M.A. Kanso and A.J. Giacomin, "Cole-Cole Relation for Long-Chain Branching from General Rigid Bead-Rod Theory," *Physics of Fluids*, **32**(9), 093106 (September, 2020). Editor's pick.

[12] Coombs, S.J., M.A. Kanso, K. El Haddad and A.J. Giacomin, "Complex Viscosity of Star-Branched Macromolecules From Analytical General Rigid Bead-Rod Theory," *Physics of Fluids*, **33**(9), 093111 (2021), pp. 1-24. Special Collection: Celebration of Robert Byron Bird (1924-2020).

[13] Coombs, S.J., "Macromolecular Branching from General Rigid Bead-Rod Theory," Master's Thesis, Chemical Engineering Department, Queen's University, Kingston, ON (2021).

[14] Giacomin, A.J., S.J. Coombs, Myong Chol Pak and Kwang Il Kim, "General Rigid Bead-Rod Theory for Steady-Shear Flow," *Physics of Fluids*, 35(8), 083111 (August, 2023), pp. 1-9.

[15] Kanso, Mona A., "Polymeric Liquid Behavior in Oscillatory Shear Flow," Masters Thesis, Polymers Research Group, Chemical Engineering Department, Queen's University, Kingston, CANADA (July 23, 2019). [PhD Candidate, Chemical Engineering Department, Polymers Research Group, Queen's University, Kingston, CANADA].

[16] Ferry, J.D., *Viscoelasticity of Polymers*, 2nd ed., Wiley, New York (1980).

[17] Gilbert, Peter Hunter, "Molecular Orientation in Large-Amplitude Oscillatory Shear (LAOS) of Complex Fluids," PhD Thesis, Polymers Research Group, Chemical Engineering Department, Queen's University, Kingston, CANADA (September 11, 2019). [NIST National Research Council (NRC) Research Associate, National Institute for Standards and Technology, Gaithersburg, MD]

[18] Piette, J.H., C . Saengow and A.J. Giacomin, "Hydrodynamic Interaction for Rigid Dumbbell Suspensions in Steady Shear Flow," *Physics of Fluids,* **31**(5), 053103 (May, 2019), pp. 1-7.

[19] Pak, M.C., K.-I. Kim, M.A. Kanso and A.J. Giacomin, "General Rigid Bead-Rod Theory With Hydrodynamic Interaction For Polymer Viscoelasticity," *Physics of Fluids*, **34**(2), Part 1, 023106 (February, 2022), pp. 1-17. Feature article.

[20] Kanso, M.A., Myong Chol Pak (박명철), Kwang-Il Kim (김광일), S.J. Coombs and A.J. Giacomin, "Hydrodynamic Interaction and Complex Viscosity of Multi-Bead Rods," *Physics of Fluids*, **34**(4), 043102 (April, 2022), pp. 1-13. Editor's pick.

[21] Gilbert, P.H. and A.J. Giacomin, "Molecular Origins of Higher Harmonics in Large-Amplitude Oscillatory Shear Flow: Shear Stress Response," *Physics of Fluids*, **28**(10), 103101 (October, 2016), pp. 1-36.

[22] Hoy, G.S, A.J. Giacomin and P.H. Gilbert, "Die Drool and Polymer Degradation," *Polymer-Plastics Technology and Engineering*, **55**(3), 242-258 (February, 2016).

[23] Gilbert, P.H. and A.J. Giacomin, "Slip Heating in Die Drool with Viscous Dissipation," *International Polymer Processing*, **30**(1), 141-146 (March, 2015).

[24] Gilbert, P.H. and A.J. Giacomin, "Slip Heating in Die Drool," *The Canadian Journal of Chemical Engineering*, **93**(3), 580-589 (March, 2015).

[25] Schmalzer, A.M. and A.J. Giacomin, "Die Drool Theory," *Journal of Polymer Engineering*, **33**(1), 1-18 (2013).

[26] Gilbert, Peter Hunter, "Slip Heating in Polymer Processing," Masters Thesis, Polymers Research Group, Chemical Engineering Department, Queen's University, Kingston, CANADA (November 27, 2014). [PhD Candidate, Chemical Engineering Dept., Polymers Research Group, Queen's University, Kingston, CANADA].

[27] Gander, Jesse D., "Die Lip Build-Up in Plastics Extrusion," Masters Thesis, University of Wisconsin, Mechanical Engineering Department, Madison, WI (September, 1997). [Senior Modeling and Simulation Project Engineer, Advanced Products Group, Oshkosh Truck Corp., Oshkosh, WI].

[28] Coombs, S.J., "Macromolecular Migration in Microfluidics," PhD Thesis Proposal, Chemical Engineering Department, Queen's University, Kingston, ON (2022).

[29] El Haddad, K., C. Aumnate, C. Saengow, M.A. Kanso, S.J. Coombs and A.J. Giacomin "Complex Viscosity of Graphene Suspensions," *Physics of Fluids*, **33**(9), 093109 (2021), pp. 1-9. Special Collection: Celebration of Robert Byron Bird (1924-2020).

[30] Singhal, D., M.A. Kanso, S.J. Coombs and A.J. Giacomin, "Complex Viscosity of Poly[n]catenanes Including Olympiadanes," *Physics of Fluids*, 34(3), Part 1, 033112 (March, 2022), pp. 1-26. Feature article.

[31] Kanso, M.A., Myong Chol Pak (박명철), Kwang-Il Kim (김광일), S.J. Coombs and A.J. Giacomin, "Hydrodynamic Interaction and Complex Viscosity of Multi-Bead Rods," *Physics of Fluids*, 34(4), 043102 (April, 2022), pp. 1-13. Editor's pick.

[32] Giacomin, A.J., S.J. Coombs, Myong Chol Pak and Kwang Il Kim, "General Rigid Bead-Rod Theory for Steady-Shear Flow," *Physics of Fluids*, 35(8), 083111 (August, 2023), pp. 1-9.

[33] Jendrejack, R.M., D.C. Schwartz, J.J. de Pablo and M.D. Graham, "Shear-Induced Migration in Flowing Polymer Solutions: Simulation of Long-Chain DNA in Microchannels," *Journal of Chemical Physics*, **120**, pp. 2513-2529 (2004).

[34] Graham, M.D., "Fluid Dynamics of Dissolved Polymer Molecules in Confined Geometries," *Annual Review of Fluid Mechanics*, **42**, pp. 273-298 (2011).

[35] Rems, L., D. Kawale, L.J. Lee and P.E. Boukany, "Flow of DNA in Micro/Nanofluidics: From Fundamentals to Applications," Biomicrofluidics, 10, 043403 (2016).

[36] Alicia, T.G.G., C. Yang, Z. Wang, N.T. Nguyen, "Combinational Concentration Gradient Confinement Through Stagnation Flow," *Lab on a Chip*, **16**, (2017), 368-376.

[37] Kirkwood, J.G. and P.L. Auer, "The Viscoelastic Properties of Solutions of Rod-Like Macromolecules," *The Journal of Chemical Physics*, **19**, 281 (1951).

[38] Kirkwood, J.G. and R.J. Plock, "Non-Newtonian Viscoelastic Properties of Rod-Like Macromolecules in Solutions," *The Journal of Chemical Physics*, **24**, 665 (1956).

[39] E.W. Paul, "Non-Newtonian Viscoelastic Properties of Rodlike Molecules in Solution: Comment on a Paper by Kirkwood and Plock," *The Journal of Chemical Physics*, **51**, 1271 (1969).

[40] E.W. Paul, "Some Non-Equilibrium Problems for Dilute Solutions of Macromolecules. Part I: The Plane Polygonal Polymer," Ph.D. Thesis, Department of Chemistry, University of Oregon, Eugene, OR (1970).

[41] Saengow, C., A.J. Giacomin and C. Kolitawong, "Exact Analytical Solution for Large-Amplitude Oscillatory Shear Flow from Oldroyd 8-Constant Framework: Shear Stress," *Physics of Fluids*, **29**(4), 043101 (April, 2017), pp. 1-23. Errata: In column 4 of rows 12 and 13 of TABLE IV., $\lambda_2 = \mu_0 = \mu_1$ should be $\mu_1 = -\lambda_1;\ \lambda_2 = \mu_0$ and $\mu_1 = \lambda_1;\ \lambda_2 = \mu_0$.

[42] Bird, R.B. and A.J. Giacomin, "Polymer Fluid Dynamics: Continuum and Molecular Approaches," *Annual Review of Chemical and Biomolecular Engineering*, **7**, 479–507 (2016).

[43] Bird, R.B., H.R. Warner, Jr. and D.C. Evens, "Kinetic theory and rheology of dumbbell suspensions with Brownian motion," *Advanced Polymer Scien*ce, **8**, 1 (1971).

[44] Kanso, M.A., A.J. Giacomin, C. Saengow and J.H. Piette, "Macromolecular Architecture and Complex Viscosity," *Physics of Fluids,* **31**(8), 087107 (August, 2019), pp. 1-28. Editor's pick.

[45] Bird, R.B., R.C. Armstrong and O. Hassager, *Dynamics of Polymeric Liquids*, Vol. 1, 1st ed., Wiley, New York (1977).

[46] Gemant, A., "Komplexe Viskosität," *Naturwissenschaften*, **23**(25), 406-407 (1935).

[47] Gemant, A., "The Conception of a Complex Viscosity and its Application to Dielectrics," *Transactions of the Faraday Society*, **31**(175, Part II), 1582-1590 (1935).

[48] Bird, R.B. and A.J. Giacomin, "Who Conceived the Complex Viscosity?," *Rheologica Acta*, **51**(6), 481-486 (2012).

[49] Hsiao, K.W., J. Dinic, Y. Ren, V. Sharma and C.M. Schroeder, "Passive Non-Linear Microrheology for Determining Extensional Viscosity," *Physics of Fluids*, **29**, (2017), pp. 1-12.

[50] Varchanis, S., C.C. Hopkins, A.Q. Shen, J. Tsamopoulos and S.J. Haward, "Asymmetric Flows of Complex Fluids Past Confined Cylinders: A Comprehensive Numerical Study with Experimental Validation," *Physics of Fluids*, **32**, (2020), pp. 1-18.

[51] Janssen, P.J.A., P.D. Anderson and M. Loewenberg, "A Slender-Body Theory for Low Viscosity Drops in Shear Flow Between Parallel Walls," *Physics of Fluids*, **22**, (2010), pp. 1-10.

[52] Park, O.O., "Dynamics of Rigid and Flexible Polymer Chains," PhD Thesis, Stanford University, Stanford, CA (June, 1985).

[53] Woo, N.J., E.S.G. Shaqfeh, B. Khomami, "Effect of Confinement on Dynamics and Rheology of Dilute DNA Solutions. I. Entropic Spring Force Under Confinement and a Numerical Algorithm," *Journal of Rheology,* **48**(2), (2004), pp. 281-298.

[54] Woo, N.J., E.S.G. Shaqfeh, B. Khomami, "Effect of Confinement on Dynamics and Rheology of Dilute Deoxyribose Nucleic Acid Solutions. II. Effective Rheology and Single Chain Dynamics," *Journal of Rheology,* **48**(2), (2004), pp. 299-318.

[55] Parisi, D., D. Truzzolillo, V.D. Deepak, M. Gauthier and D. Vlassopoulos, "Transition From Confined to Bulk Dynamics in Symmetric Star-Linear Polymer Mixtures," *Macromolecules,* **52**, (2019), pp. 5872-5883.

[56] Leungo, G., F.J. Schmitt, R. Hill and J. Israelachvili, "Thin Film Rheology and Tribology of Confined Polymer Melts: Contrasts with Bulk Properties," *Macromolecules*, **30**, (1997), pp. 2482-2494.

[57] Davies, G.A. and J.R. Stokes, "Thin Film and High Shear Rheology of Multiphase Complex Fluids," *Journal of Non-Newtonian Fluid Mechanics*, **148**, (2008), pp. 73-87.

[58] Costanzo, S., R. Pasquino, J. Läuger and N. Grizzuti, "Milligram Size Rheology of Molten Polymers," *Fluids*, **4**(1) (2019), pp. 1-11.

[59] Magda, J.J. and S.G. Baek, "Concentrated Entangled and Semidilute Entangled Polystyrene Solutions and the Second Normal Stress Difference," *Polymer*, **35**(6) (1994), pp. 1187-1194.

[60] Bueche, F. and M. Davison, "Viscosity-Temperature Relation for Diethyl Phthalate," *Journal of Chemical Physics*, **45**(11) (1966), pp. 4361-4362.

[61] Nguyen, X.D., H.J. Jeon, H.Y. Kim, H.J. Paik, J. Huh, H.H. Kim and J.S. Go, "Microfluidic Separation of a Soluble Substance Using Transverse Diffusion in a Layered Flow," *Micromachines*, **8**(9), pp. 1-10 (2016)

[62] Jendrejack, R.M., D.C. Schwartz, M.D. Graham and J.J. de Pablo, "Effect of Confinement on DNA Dynamics in Microfluidic Devices," *Journal of Chemical Physics*, **119**(2), (2003), pp. 1165-1173.

[63] Hernández-Ortiz, J.P., J.J. de Pablo and M.D. Graham, "Fast Computation of Many-Particle Hydrodynamic and Electrostatic Interactions in a Confined Geometry," *Physical Review Letters*, **98**(14), 140602 (2007), pp. 140602-140602.

[64] Lauricella, G., J. Zhou, Q. Luan, I. Papautsky and Z. Peng, "Computational Study of Inertial Migration of Prolate Particles in a Straight Rectangular Channel," *Physics of Fluids*, **34**, 082021(2022), pp. 1-11.

[65] R. B. Bird, C. F. Curtiss, R. C. Armstrong, and O. Hassager, Dynamics of Polymeric Liquids, 2nd ed. (Wiley, New York, 1987), Vol. 2.

[66] Piette, J.H., C. Saengow and A.J. Giacomin, "Zero-Shear Viscosity of Fraenkel Dumbbell Suspensions," *Physics of Fluids*, **32**(6), 063103 (June, 2020), pp. 1-11.

[67] N. Thrien, B. Coupal, and J. L. Corneille, *Can. J. Chem. Eng*. 48, 17 (1970).

[68] G. Astarita, G. Marrucci, and G. Palumbo, *Ind. Eng. Chem. Fundamentals 3*, 333 (1964).

[69] Dealy, J.N. and K.F. Wissbrun, *Melt Rheology and its Role in Plastics Processing: Theory and Applications,* Van Nostrand, New York (1990).

[70] Giacomin, A.J., R.B. Bird, L.M. Johnson and A.W. Mix, "Large-Amplitude Oscillatory Shear Flow from the Corotational Maxwell Model," *Journal of Non-Newtonian Fluid Mechanics*, **166**(19-20), 1081–1099 (2011).

[71] Saengow, C. and A.J. Giacomin, "Exact Solutions for Oscillatory Shear Sweep Behaviors of Complex Fluids from the Oldroyd 8-Constant Framework," *Physics of Fluids*, **30**(3), 030703 (March, 2018), pp. 1-21.

[72] Giacomin, A.J., R.B. Bird, L.M. Johnson and A.W. Mix,'Corrigenda: "Large-Amplitude Oscillatory Shear Flow from the Corotational Maxwell Model," [Journal of Non-Newtonian Fluid Mechanics, **166**, 1081–1099 (2011)],' *Journal of Non-Newtonian Fluid Mechanics*, **187-188**, 48-48 (2012).

[73] R. B. Bird, O. Hassager, R. C. Armstrong and C. F. Curtiss, Dynamics of Polymeric Liquids, 1st ed. (John Wiley and Sons, Inc., New York, 1977), Vol. 2.

[74] Shrimal, P., G. Jadeja and S. Patel, "A Review on Novel Methodologies for Drug Nanoparticle Preparation: Microfluidic Approach," *Chemical Engineering Research and Design*, **153**, pp. 728-756 (2020).

[75] Song, Y., J. Hormes and C.S.S.R. Kumar, "Microfluidic Synthesis of Nanomaterials," *Small*, **4**, pp. 698-711 (2008).

[76] Pan, L.J., J.W. Tu, H.T Ma, Y.J. Yang, Z.Q. Tian, D.W. Pang and Z.L. Zhang, "Controllable Synthesis of Nanocrystals in Droplet Reactors," *Lab on a Chip*, **18**, 41-56 (2018).

[77] Nguygen N.T. and Z. Wu, "Micromixers—A Review," *Journal of Micromechanics and Microengineering*, **15**(2), (2005).

[78] Hessel, V., H. Löwe and F. Schönfeld, "Micromixers—A Review on Passive and Active Mixing Principles," *Chemical Engineering Science*, **60**(8-9) pp. 2479-2501 (2005).

[79] Suh, Y.K. and S. Kang, "A Review on Mixing in Microfluidics," *Micromachines*, **1**(3), pp. 82-111 (2010).

[80] Cai, G., L. Xue, H. Zhang and J. Lin, "A Review on Micromixers," *Micromachines*, **8**(9), pp.274 (2017).

[81] Wongkaew, N., M. Simsek, C. Griesche and A.J. Baeumner, "Functional Nanomaterials and Nanostructures Enhancing Electrochemical Biosensors and Lab-on-a-Chip Performances: Recent Progress, Applications, and Future Perspective," *Chemical Reviews*, **119**(1), pp. 120-194 (2019).

[82] Sengupta, P., K. Khanra, A.R. Chowdhury, P. Datta, "4 – Lab-on-a-chip Sensing Devices for Biomedical Applications," *Bioelectronics and Medical Devices*, pp. 47-95 (2019).

[83] Shi, H., K. Nie, B. Dong, M. Long, H. Xu and Z. Liu, "Recent Progress of Microfluidic Reactors for Biomedical Applications," *Chemical Engineering Journal*, **361**(4), pp. 635-650 (2019).

[84] Hamdallah, S.I., R. Zoqlam, P. Erfle, M. Blyth, A.M. Alkilany, A. Dietzel and S. Qi, "Microfluidics for Pharmaceutical Nanoparticle Fabrication: The Truth and the Myth," *International Journal of Pharmaceutics*, **584**(6), 119408 (2020).

[85] Sun, W., Z. Luo, J. Lee, H.-J. Kim, K.J. Lee, P. Tebon, Y. Feng, M.R. Dokmeci, S. Sengupta, A. Khademhosseini, "Organ-on-a-Chip for Cancer and Immune Organs Modeling," *Advanced Healthcare Materials,* **8**(4), 1801363 (2019).

[86] Moradi, E., S. Jalili-Firoozinezhad and M. Solati-Hashjin, "Microfluidic Organ-on-a-Chip Models of Human Liver Tissue," *Acta Biomaterialia*, **116**, pp. 67-83 (2020).

[87] D'Avino, G., F. Greco and P. L. Maffettone, "Particle Migration Due to Viscoelasticity of the Suspending Liquid and its Relevance in Microfluidic Devices," *Annual Review of Fluid Mechanics*, **49**, pp. 341-360 (2017).

[88] Leshansky, A.M., A. Bransky, N. Korin, and U. Dinnar, "Tunable Nonlinear Viscoelastic "Focusing" in a Microfluidic Device," *Physical Review Letters*, **98**, 234501 (2007).

[89] Di Carlo, D., D. Irimia, R. G. Tompkins and M. Toner, "Continuous Inertial Focusing, Ordering, and Separation of Particles in Microchannels," *Proceedings of the National Academy of Sciences of the United States of America*, **104**(48), 18892 (2007).

[90] Yang, S., J.Y. Kim, S.J. Lee, S.S. Lee and J.M. Kim, "Sheathless Elasto-Inertial Particle Focusing and Continuous Separation in a Straight Rectangular Microchannel," *Lab on a Chip*, **11**(2), 266 (2011).

[91] Seo, K.W., Y.J. Kang and S.J. Lee, "Lateral Migration and Focusing of Microspheres in a Microchannel Flow of Viscoelastic Fluids," *Physics of Fluids*, **26**(6), 063301 (2014).

[92] Yu, Z., P. Wang, J. Lin and H.H. Hu, "Equilibrium Positions of the Elasto-Inertial Particle Migration in Rectangular Channel Flow of Oldroyd-B Viscoelastic Fluids," *Journal of Fluid Mechanics*, 868, pp. 316-340 (2019).

[93] Fedosov, D.A. and G. Gompper, "White Blood Cell Margination in Microcirculation," *Soft Matter*, **10**, pp. 2961-2970 (2014).

[94] Secomb, T.W., "Blood Flow in the Microcirculation," *Annual Review of Fluid Mechanics*, **49**, pp. 443-461 (2017).

[95] Shevkoplyas, S.S., T. Yoshida, L.L. Munn and M.W. Bitensky, "Biomimetic Autoseparation of Leukocytes from Whole Blood in a Microfluidic Device," *Analytical Chemistry*, **77**(3), pp. 933-937 (2005).

[96] Oh, D., S. Ii and S. Takagi, "Numerical Study of Particle Margination in a Square Channel Flow with Red Blood Cells," *Fluids*, **7**(3), 96 (2022).

[97] Carboni, E.J., B.H. Bognet, G.M. Bouchillon, A.L. Kadilak, L.M. Shor, M.D. Ward and A.W.K. Ma, "Direct Tracking of Particles and Quantification of Margination in Blood Flow," *Biophysical Journal*, **111**(7), pp. 1487-1495 (2016).

[98] Tirrell, M. and M.F. Malone, "Stress-Induced Diffusion of Macromolecules," *Journal of Polymer Science*, **15**(9), pp.1569-1583 (1977).

[99] Niculescu, A-.G., C. Chircov, A.C. Bîca and A.M. Grumezescu, "Fabrication and Applications of Microfluidic Devices: A Review," *International Journal of Molecular Sciences*, **22**(4), (2011).

[100] Scott, S.M and Z. Ali, "Fabrication Methods for Microfluidic Devices: An Overview," *Micromachines*, **12**(3) 319 (2021).

[101] Kim. P., K.W. Kwon, M.C. Park, S.H. Lee, S.M. Kim and K.Y. Suh, "Soft Lithography for Microfluidics: A Review," *Biochip Journal*, **2**(1), pp. 1-11 (2008).

[102] Fallahi, H., J. Zhang, H-.P. Plan and N-.T. Nguyen, "Flexible Microfluidics: Fundamentals, Recent Developments, and Applications," *Micromachines*, **10**, pp. 830 (2019).

[103] L.D.S. Yadav, Organic Spectroscopy, 1st ed. (Spring Science+Business Media Dordrecht, 2005), Vol. 2.

[104] Mayerhöfer, T.G., A.V. Pipa and J. Popp, "Beer's Law-Why Integrated Absorbance Depends Linearly on Concentration," *Chemphyschem*, **20**(21), pp.2748-2753 (2019).

[105] Bradley, B., J. Gomez-Cruz and C. Escobedo, "Integrated Microfluidic-Electromagnetic System to Probe Single-Cell Magnetotaxis in Microconfinement," *Bioengineering*, **10**, 1034 (2023).

[106] Class, N.R., R. Tjeung, P. Chan, L.Y. Yeo and J.R. Friend, "Organosilane Deposition for Microfluidic Application," *Biomicrofluidics*, **5**(3), pp. 036501-036507 (2011).

[107] Venzac, B., S. Deng, Z. Mahmoud, A. Lenferink, A. Costa, F. Bray, C. Otto, C. Rolando and D. Le Gac, "PDMS Curing Inhibition on 3D-Printed Molds: Why? Also, How to Avoid It?," *Analytical Chemistry*, **93**(19), pp. 7180-7187 (2021).

[108] Borók, A., K. Laboda and A. Bonyár, "PDMS Bonding Technologies for Microfluidic Applications: A Review," *Biosensors*, **11**(8), 292 (2021).

[109] Lee, J.N., C. Park and G.M. Whitesides, "Solvent Compatibility of Poly(dimethylsiloxane)-Based Microfluidics Devices," *Analytical Chemistry*, **75**(23), pp. 6544-6554 (2003).

[110] Li, T., C. Zhou, and M. Jiang, "UV Absorption Spectra of Polystyrene,". *Polymer Bulletin* **25**, pp. 211–216 (1991).

[111] Schmalzer, A.M., R.B. Bird and A.J. Giacomin, "Normal Stress Differences in Large-Amplitude Oscillatory Shear Flow for Dilute Rigid Dumbbell Suspensions," *Journal of Non-Newtonian Fluid Mechanics*, **222**, 56-71 (2015). Errata: In Eq. (6), "38725" should be "38728"; Above Eqs. (14) and (25), "significant figures" should be "16 significant figures".

[112] Piette, J.H., L.M. Jbara, C. Saengow and A.J. Giacomin, "Exact Coefficients for Rigid Dumbbell Suspensions for Steady Shear Flow Material Function Expansions," *Physics of Fluids*, **31**(2), 021212 (2019), pp. 1-15. Erratum: Above Eq. (83), "one other" should be "one other use".

[113] Nisisako, T., T. Ando and T. Hatsuzawa, "High-volume Production of Single and Compound Emulsions in a Microfluidic Parallelization Arrangement Coupled with Coaxial Annular World-to-Chip Interfaces," *Lab Chip*, **12**, (2012), pp. 3426-3435.

[114] O. Hassager, "Kinetic theory and rheology of bead-rod models for macromolecular solutions. II. Linear unsteady flow properties," J. Chem. Phys. **60**(10), 4001–4008 (1974).

[115] Piette, J.H., C . Saengow and A.J. Giacomin, "Hydrodynamic Interaction for Rigid Dumbbell Suspensions in Steady Shear Flow," *Physics of Fluids,* **31**(5), 053103 (May, 2019), pp. 1-7.

[116] Alan Jeffrey Giacomin, "Referee Acknowledgment for 2022," *Physics of Fluids,* March 2023, **35**(3), 030201.

[117] El Haddad, K., C. Aumnate, C. Saengow, M.A. Kanso, S.J. Coombs and A.J. Giacomin "Complex Viscosity of Graphene Suspensions," *Physics of Fluids*, **33**(9), 093109 (2021), pp. 1-9. Special Collection: Celebration of Robert Byron Bird (1924-2020).

[118] Singhal, D., M.A. Kanso, S.J. Coombs and A.J. Giacomin, "Complex Viscosity of Poly[n]catenanes Including Olympiadanes," *Physics of Fluids*, 34(3), Part 1, 033112 (March, 2022), pp. 1-26. Feature article.

[119] Coombs, Steacy Jacqueline, "Macromolecular Branching from General Rigid Bead-Rod Theory," Masters Thesis, Polymers Research Group, Chemical Engineering Department, Queen's University, Kingston, CANADA (July 31, 2021). [PhD Candidate, Chemical Engineering Department, Polymers Research Group, Queen's University, Kingston, CANADA].